Universität Karlsruhe (TH)
Institut für Baustatik

A geometrically nonlinear piezoelectric solid shell element based on a mixed multi-field variational formulation

S. Klinkel, W. Wagner

Mitteilung 3(2005)

Universität Karlsruhe (TH)
Institut für Baustatik

A geometrically nonlinear piezoelectric solid shell element based on a mixed multi-field variational formulation

S. Klinkel, W. Wagner

Mitteilung 3(2005)

Prof. Dr.–Ing. W. Wagner
Institut für Baustatik
Universität Karlsruhe
Postfach 6980
76128 Karlsruhe

Telefon: (0721) 608–2280
Telefax: (0721) 608–6015
E–mail: bs@.uni-karlsruhe.de
Internet: http://www.bs.uni-karlsruhe.de

A geometrically nonlinear piezoelectric solid shell element based on a mixed multi-field variational formulation

S. Klinkel, W. Wagner

Institut f. Baustatik, Universität Karlsruhe (TH), Kaiserstr. 12, Karlsruhe, 76131, Germany

Abstract

This paper is concerned with a geometrically nonlinear solid shell element to analyze piezoelectric structures. The finite element formulation is based on a variational principle of the Hu-Washizu type and includes six independent fields: displacements, electric potential, strains, electric field, mechanical stresses and dielectric displacements. The element has 8 nodes with 4 nodal degrees of freedoms, 3 displacements and the electric potential. A bilinear distribution through the thickness of the independent electric field is assumed to fulfill the electric charge conservation law in bending dominated situations exactly. The presented finite shell element is able to model arbitrary curved shell structures and incorporates a 3D-material law. A geometrically nonlinear theory allows large deformations and includes stability problems. Linear and nonlinear numerical examples demonstrate the ability of the proposed model to analyze piezoelectric devices.

keywords: piezoelectricity, solid shell element, mixed finite element formulation, smart structures

1 Introduction

In the last decade smart materials and structures are increasingly applied to sensors and actuators in the field of precision systems and mechatronic and structronic systems, see e.g. [1] and references therein. Smart structural systems refer to a wide range of active materials. This paper is restricted to piezoelectric materials. Piezoelectric devices have an extensive variety of applications, which include micro electro mechanical systems (MEMS), see e.g. [2, 3], up to applications to large civil infrastructures, see [4].

Since the pioneering work of Allik and Hughes [5] many finite elements have been developed to analyze piezoelectric structural elements. A survey

of mechanical models and finite element formulations for piezoelectric beam, plate, shell and brick structures are presented in [6, 7].

In recent years several new shell elements have been proposed, where piezoelectric constitutive relations have been included in the underlying element formulation. Some of these elements model a reference surface of the shell structure, see e.g. [8, 9, 10, 11, 12, 13, 14], to mention a few. Several of these element formulations are restricted to shallow shell structures, [12, 13, 14], where the initial shell curvature is assumed to be small. Due to the fact that the piezoelectric devices have traditionally laminate forms, the above mentioned shell formulations include a more or less sophisticated laminate theory. A survey of different laminate theories is given in [6]. The so-called solid shell elements circumvent complicated laminate theories by modeling the top and the bottom surface of shell structures. For each ply in a laminate one element is employed in thickness direction. Different shear deformations for each layer are allowed. Piezoelectric solid shell elements were proposed in e.g. [15, 16, 17, 18, 19, 20].

All of the above cited piezoelectric shell formulations except [12] assume a geometrically linear theory for the shell kinematics. In the theoretical contributions of Tzou [21, 22] it is pointed out that nonlinear characteristics can significantly influence the performance of piezoelectric structures and systems. Pai et al. [23] investigate nonlinear dynamics with piezoelectric plates, where geometric nonlinearities lead to flutter and chaotic vibrations. Nonlinear piezoelectric circular shells with large amplitudes on the vibrating frequency are discussed in [24]. Geometrically nonlinear effects like buckling of plates and snap-through were analyzed in [22, 12]. The most nonlinear piezoelectric plate formulations [25, 21, 22, 24, 12, 26] use von Karman plate theory to account for geometric nonlinearities. The von Karman theory is a nonlinear theory of lowest order and does not cover all geometric nonlinearities. Due to the use of linear expressions for the curvature deformation the von Karman strains are restricted to moderate rotations. A geometrically nonlinear theory which incorporates large rotations is presented in [23], which is limited to piezoelectric plates.

In the most of the piezoelectric models the electric field inside the actuator or sensor is assumed to be constant, which is in bending dominated situations not correct. Yang [27] showed that higher order potential variations through the thickness in a piezoelectric plate theory are necessary to capture the bending effects. On the basis of a first order shear deformation theory a quadratic assumption of the electric potential through the beam

thickness is discussed in [28]. In the work on piezoelectric plates Benjeddou et al. [29] emphasized that a quadratic electric potential through the plate thickness satisfies the electric charge conservation law exactly. In finite element formulations for shells a quadratic approximation of the electric potential through the shell thickness is recently introduced in [8, 9, 10, 11]. A quadratic approximation leads in general to additional degrees of freedom. This holds also for [13], in which a hybrid finite shell formulation with degrees of freedom for the electric potential and the dielectric displacements is proposed to fulfill the electric charge conservation law.

Hybrid and mixed approaches are also presented in [30, 31, 16, 17]. Miranda and Ubertini [30] discuss the fully compatible approach in comparison to a hybrid approach. For the hybrid approach they introduced a functional with four fields, the displacement, the mechanical stresses, the electric potential, and the electric displacements as independent variables. The electric field and the strains are derived from the constitutive equations. Sze and Pan [31] consider the most general variational principle which includes six field variables. Form this general principle they degenerate some variational formulations by eliminating some of the independent fields. The degenerated variational principles are employed to the finite element formulation. Sze and Yao [16, 17] proposed a hybrid finite element shell formulation for smart structures modelling. In [16, 17] three fields, the stress field, the displacements, and the electric potential are considered in the variational formulation, where the electric potential is assumed to be linear through the shell thickness.

In this paper a solid shell element for piezoelectric is presented. The main features and novel aspects are summarized as follows:

- The finite element formulation is based on the most general variational formulation principle of the Hu-Wahizu type and includes six independently assumed field variables. The variables are the stress field, the strain field, the displacements, the electric displacements, the electric field, and the electric potential. Each field is incorporated in the finite element formulation and is approximated with appropriate interpolations on element level.

- The electric potential is assumed to be linear through the shell thickness, which is in bending dominated situations not correct, as discussed above. To get correct results a bilinear approximation of the electric

field through the shell thickness is assumed. This implicates an exact fulfillment of the charge conservation law in bending dominated situations. The bilinear approximation leads to additional internal degrees of freedom, which are eliminated by a static condensation on element level. No extra global degrees of freedoms appear in the presented finite element formulation. Furthermore it will be shown that a bilinear approximation is necessary to pass the important out of plane bending patch test.

- A complete geometrically nonlinear theory is presented. It allows large deformations and accounts for snap-through effects and stability problems. Due to the assumption of the linear constitutive equations, the model is only restricted to small strains.

- The presented finite shell element is able to model arbitrary curved shell structures and it is not restricted to shallow shells.

- The shell formulation incorporates a three-dimensional material law. There are no assumptions regarding the stress state and the admissible electric displacements on element level. Some common simplifying assumptions for the electric displacements are currently under discussion, if they are in accordance to dynamic investigations, see e.g. [28]. Moreover the use of a three-dimensional material law is advantageous if material nonlinearities like domain switching effects should be implemented in the underlying shell formulation, see e.g. [32].

- To improve the behavior of the low order hexahedral element some assumed natural strain interpolations, see [33], [34], are employed in the finite element formulation. Furthermore it is noted that a part of the independently assumed strains are interpolated in the same manner as proposed by Simo and Rifai [35].

The outline of the paper is as follows: In Section 2 we introduce the gradient fields in a curvilinear description. For the strain measure a geometrically nonlinear kinematic assumption is employed. In Section 3 the constitutive relations between the stresses, dielectric displacements, the mechanical strains, and the electric field are presented. The variational principle is introduced in Section 4. Section 5 is concerned with the mixed finite element approximation. Section 6 provides the dynamic field problem and the

discrete approximation in time. In Section 7 some linear and nonlinear numerical examples demonstrate the ability of the proposed model to analyze piezoelectric devices.

2 Gradient fields

In this Section the nonlinear Green-Lagrangean strains and the electric field are derived in convective coordinates. The parameters ξ^1, ξ^2 are defined as in-plane coordinates and ξ^3 as thickness coordinate of the considered shell formulation. The position vector of the reference configuration $\mathcal{B}_0$ and the current configuration $\mathcal{B}_t$ are denoted by $\boldsymbol{X}$ and $\boldsymbol{x} = \boldsymbol{X} + \boldsymbol{u}$, where $\boldsymbol{u}$ is the displacement vector. The covariant tangent vectors are defined as

$$\boldsymbol{G}_i = \frac{\partial \boldsymbol{X}}{\partial \xi^i} \ , \quad \boldsymbol{g}_i = \frac{\partial \boldsymbol{x}}{\partial \xi^i} \ , \quad i = 1, 2, 3 \quad . \tag{1}$$

The contravariant basis vectors are defined by the orthogonality $\boldsymbol{G}_i \cdot \boldsymbol{G}^j = \delta_i^j$ and $\boldsymbol{g}_i \cdot \boldsymbol{g}^j = \delta_i^j$, respectively. The deformation gradient is a map of the tangent spaces $\boldsymbol{F}(\boldsymbol{X}) : \boldsymbol{T}\mathcal{B}_0 \rightarrow \boldsymbol{T}\mathcal{B}_t$ and is given in convective description as

$$\boldsymbol{F} = \frac{\partial \boldsymbol{x}}{\partial \boldsymbol{X}} = \boldsymbol{g}_i \otimes \boldsymbol{G}^i \quad , \tag{2}$$

where the summation convention on repeated indices is assumed. Introducing the metric coefficients $g_{ij} = \boldsymbol{g}_i \cdot \boldsymbol{g}_j$ and $G_{ij} = \boldsymbol{G}_i \cdot \boldsymbol{G}_j$ the components of the Green-Lagrangean strain measure read

$$E_{ij} = \frac{1}{2}(g_{ij} - G_{ij}) \quad , \tag{3}$$

and are arranged in a vector $\boldsymbol{E}_{cova} = [E_{11},\, E_{22},\, E_{33},\, 2E_{12},\, 2E_{13},\, 2E_{23}]^T$. Introducing

$$\boldsymbol{T} = \begin{bmatrix} (J_{11})^2 & (J_{12})^2 & (J_{13})^2 & aJ_{11}J_{12} & aJ_{11}J_{13} & aJ_{12}J_{13} \\ (J_{21})^2 & (J_{22})^2 & (J_{23})^2 & aJ_{21}J_{22} & aJ_{21}J_{23} & aJ_{22}J_{23} \\ (J_{31})^2 & (J_{32})^2 & (J_{33})^2 & aJ_{31}J_{32} & aJ_{31}J_{33} & aJ_{32}J_{33} \\ bJ_{11}J_{21} & bJ_{12}J_{22} & bJ_{13}J_{23} & J_{11}J_{22} + J_{12}J_{21} & J_{11}J_{23} + J_{13}J_{21} & J_{12}J_{23} + J_{13}J_{22} \\ bJ_{11}J_{31} & bJ_{12}J_{32} & bJ_{13}J_{33} & J_{11}J_{32} + J_{12}J_{31} & J_{11}J_{33} + J_{13}J_{31} & J_{12}J_{33} + J_{13}J_{32} \\ bJ_{21}J_{31} & bJ_{22}J_{32} & bJ_{23}J_{33} & J_{21}J_{32} + J_{22}J_{31} & J_{21}J_{33} + J_{23}J_{31} & J_{22}J_{33} + J_{23}J_{32} \end{bmatrix} , \tag{4}$$

a transformation matrix is defined as

$$\boldsymbol{T}_S = \boldsymbol{T} \quad \text{with} \quad a = 2, \quad b = 1 \quad , \tag{5}$$

where $J_{ik} = \boldsymbol{t}_i \cdot \boldsymbol{G}_k$ and $\boldsymbol{t}_1 = \frac{\boldsymbol{G}_1}{\|\boldsymbol{G}_1\|}$, $\boldsymbol{t}_2 = \frac{\boldsymbol{G}_3 \times \boldsymbol{G}_1}{\|\boldsymbol{G}_3 \times \boldsymbol{G}_1\|}$, $\boldsymbol{t}_3 = \boldsymbol{t}_1 \times \boldsymbol{t}_2$. The transformation to the local orthonormal basis system $\boldsymbol{t}_i$ is given as

$$\boldsymbol{E} = \boldsymbol{T}_S^{-T} \, \boldsymbol{E}_{cova} \quad . \tag{6}$$

A material description of the electric field, also known as Lagrangean electric field, see Maugin [36], is given as

$$\vec{\boldsymbol{E}} = -\frac{\partial \varphi}{\partial \xi^i} \, \boldsymbol{G}^i \quad , \tag{7}$$

here φ denotes the electric potential. The covariant components $-\frac{\partial \varphi}{\partial \xi^i}$ are arranged in a vector $\vec{\boldsymbol{E}}_{cova} = [\vec{E}_1, \vec{E}_2, \vec{E}_3]^T$. The physical electrical field in spatial description is obtained as $\vec{\boldsymbol{e}} = \vec{\boldsymbol{E}} \boldsymbol{F}^{-1}$. If it is not otherwise noted we refer always to the Lagrangian electric field. With the Jacobian matrix

$$\boldsymbol{J} = \begin{bmatrix} J_{11} & J_{12} & J_{13} \\ J_{21} & J_{22} & J_{23} \\ J_{31} & J_{32} & J_{33} \end{bmatrix} \quad , \tag{8}$$

the transformation to the local orthonormal basis system is determined by

$$\vec{\boldsymbol{E}} = \boldsymbol{J}^{-1} \vec{\boldsymbol{E}}_{cova} \quad . \tag{9}$$

3 Constitutive equations

To present a compact form of the constitutive relations, the strains $\boldsymbol{E}$, the electric field $\vec{\boldsymbol{E}}$ as well as the second Piola-Kirchhoff stresses $\boldsymbol{S}$ and the material dielectric displacements $\vec{\boldsymbol{D}}$ are arranged in vectors

$$\boldsymbol{\varepsilon} = \begin{bmatrix} \boldsymbol{E} \\ \vec{\boldsymbol{E}} \end{bmatrix} \quad , \quad \boldsymbol{\sigma} = \begin{bmatrix} \boldsymbol{S} \\ -\vec{\boldsymbol{D}} \end{bmatrix} \quad . \tag{10}$$

The dielectric displacements in spatial description read $\vec{\boldsymbol{D}} = \det \boldsymbol{F} \, \vec{\boldsymbol{d}} \boldsymbol{F}^{-T}$. If it is not otherwise denoted we refer always to the Lagrangian dielectric displacements.

The relation between the material quantities $\boldsymbol{S}$, $\vec{\boldsymbol{D}}$ and the Lagrangian gradient fields $\boldsymbol{E}$, $\vec{\boldsymbol{E}}$ is assumed to be linear, see e.g. [36, 37] and is given as

$$\boldsymbol{\sigma} = \mathbb{D}\,\boldsymbol{\varepsilon} \quad . \tag{11}$$

The constitutive model is identical to Voigt's linear theory of piezoelectricity, but here we define a nonlinear strain measure and therefore we have to distinguish between spatial and material quantities. The constant material matrix $\mathbb{D}$ reads

$$\mathbb{D} = \begin{bmatrix} \mathbb{C} & -\mathbb{e} \\ -\mathbb{e}^T & -\boldsymbol{\epsilon} \end{bmatrix} \quad , \tag{12}$$

where $\mathbb{C}$ is the elasticity matrix, $\mathbb{e}$ the piezoelectric matrix and $\boldsymbol{\epsilon}$ the permittivity matrix. With respect to the local orthonormal basis system $\boldsymbol{t}_i$ the inverse elasticity matrix is given for orthotropic materials as

$$\mathbb{C}^{-1} = \begin{bmatrix} \frac{1}{E_1} & -\frac{\nu_{12}}{E_2} & -\frac{\nu_{13}}{E_3} & 0 & 0 & 0 \\ -\frac{\nu_{12}}{E_2} & \frac{1}{E_2} & -\frac{\nu_{23}}{E_3} & 0 & 0 & 0 \\ -\frac{\nu_{13}}{E_3} & -\frac{\nu_{23}}{E_3} & \frac{1}{E_3} & 0 & 0 & 0 \\ 0 & 0 & 0 & \frac{1}{G_{12}} & 0 & 0 \\ 0 & 0 & 0 & 0 & \frac{1}{G_{13}} & 0 \\ 0 & 0 & 0 & 0 & 0 & \frac{1}{G_{23}} \end{bmatrix} \quad , \tag{13}$$

here the Young's moduli E_1, E_2, E_3, the Poisson's ratios ν_{12}, ν_{13}, ν_{23} and the shear moduli G_{12}, G_{13}, G_{23} are independent material parameters, which are defined below in the Section numerical examples. Relating to $\boldsymbol{t}_i$ the piezoelectric matrix $\mathbb{e}$ and the permittivity matrix $\boldsymbol{\epsilon}$ read

$$\mathbb{e} = \begin{bmatrix} 0 & 0 & \mathbb{e}_{13} \\ 0 & 0 & \mathbb{e}_{23} \\ 0 & 0 & \mathbb{e}_{33} \\ 0 & 0 & 0 \\ \mathbb{e}_{51} & 0 & 0 \\ 0 & \mathbb{e}_{62} & 0 \end{bmatrix} \quad , \quad \boldsymbol{\epsilon} = \epsilon \begin{bmatrix} 1 & 0 & 0 \\ 0 & 1 & 0 \\ 0 & 0 & 1 \end{bmatrix} \quad . \tag{14}$$

The stored energy function is defined as

$$W_0 = \frac{1}{2}\,\boldsymbol{\varepsilon}^T \mathbb{D} \boldsymbol{\varepsilon} \quad . \tag{15}$$

4 Variational formulation

In this Section a variational functional of the Hu-Washizu type with six independent fields is introduced as

$$\begin{aligned}\Pi(\boldsymbol{u},\,\varphi,\,\widetilde{\boldsymbol{S}},\,\widetilde{\vec{\boldsymbol{D}}},\,\bar{\boldsymbol{E}},\,\bar{\vec{\boldsymbol{E}}}) = & \int_{\mathcal{B}_0}\left[W_0(\bar{\boldsymbol{\varepsilon}}) - \widetilde{\boldsymbol{\sigma}}\cdot(\bar{\boldsymbol{\varepsilon}}-\boldsymbol{\varepsilon})\right]\,\mathrm{d}V \\ & - \int_{\mathcal{B}_0}\boldsymbol{b}\cdot\boldsymbol{u}\,\mathrm{d}V - \int_{\partial_t\mathcal{B}_0}\boldsymbol{t}\cdot\boldsymbol{u}\,\mathrm{d}A \\ & + \int_{\mathcal{B}_0} r\,\varphi\,\mathrm{d}V + \int_{\partial_q\mathcal{B}_0} q\,\varphi\,\mathrm{d}A \quad ,\end{aligned} \tag{16}$$

where

$$\bar{\boldsymbol{\varepsilon}} = \begin{bmatrix}\bar{\boldsymbol{E}}\\ \bar{\vec{\boldsymbol{E}}}\end{bmatrix} \quad , \quad \widetilde{\boldsymbol{\sigma}} = \begin{bmatrix}\widetilde{\boldsymbol{S}}\\ -\widetilde{\vec{\boldsymbol{D}}}\end{bmatrix} \tag{17}$$

are functions of the independently assumed quantities $\widetilde{\boldsymbol{S}}$, $\widetilde{\vec{\boldsymbol{D}}}$, $\bar{\boldsymbol{E}}$, and $\bar{\vec{\boldsymbol{E}}}$. The body force $\boldsymbol{b}$ is defined in the reference configuration $\mathcal{B}_0$ and $\boldsymbol{t}$ is the prescribed traction vector on the boundary $\partial_t\mathcal{B}_0$. The electric surface charge q is given on the boundary $\partial_q\mathcal{B}_0$ and the electric charge density r is defined in the body $\mathcal{B}_0$. As usual we assume that $\partial\mathcal{B}_0 = \partial_t\mathcal{B}_0 \cup \partial_u\mathcal{B}_0$ and $\partial\mathcal{B}_0 = \partial_q\mathcal{B}_0 \cup \partial_\varphi\mathcal{B}_0$, where $\partial_u\mathcal{B}_0$ denotes the boundary with prescribed values for $\boldsymbol{u}$ and $\partial_\varphi\mathcal{B}_0$ is the boundary with given values for φ, respectively.

Let $\mathcal{U} := \{\delta\boldsymbol{u} \in [H^1(\mathcal{B}_0)]^3\ \delta\boldsymbol{u}|_{\partial_u\mathcal{B}_0} = 0\}$ be the space of admissible displacement variations and $\mathcal{V} := \{\delta\varphi \in [H^1(\mathcal{B}_0)]^3\ \delta\varphi|_{\partial_\varphi\mathcal{B}_0} = 0\}$ be the space of admissible electric potential variations. Further let $\widetilde{\mathcal{S}} = \bar{\mathcal{E}} = [L_2(\mathcal{B}_0)]$ the spaces of admissible variations of the variables $\widetilde{\boldsymbol{\sigma}}$, $\bar{\boldsymbol{\varepsilon}}$. It is noted, that the space $L_2(\mathcal{B}_0)$ does not enforce inter-element continuity, when constructing the finite element approximations. The first variation reads

$$\begin{aligned}\delta\Pi = & \int_{\mathcal{B}_0}\delta\bar{\boldsymbol{\varepsilon}}\cdot\big(\frac{\partial W_0}{\partial\bar{\boldsymbol{\varepsilon}}} - \widetilde{\boldsymbol{\sigma}}\big)\,\mathrm{d}V + \int_{\mathcal{B}_0}\delta\widetilde{\boldsymbol{\sigma}}\cdot\big(\boldsymbol{\varepsilon}-\bar{\boldsymbol{\varepsilon}}\big)\,\mathrm{d}V \\ & + \int_{\mathcal{B}_0}\left[\delta\boldsymbol{\varepsilon}\cdot\widetilde{\boldsymbol{\sigma}} - \delta\boldsymbol{u}\cdot\boldsymbol{b} + \delta\varphi\,r\right]\mathrm{d}V \\ & - \int_{\partial_t\mathcal{B}_0}\delta\boldsymbol{u}\cdot\boldsymbol{t}\,\mathrm{d}A + \int_{\partial_q\mathcal{B}_0}\delta\varphi\,q\,\mathrm{d}A \;= 0 \quad .\end{aligned} \tag{18}$$

The variation of the strains and the electric field result in

$$\delta E_{ij} = \frac{1}{2}\big(\frac{\partial\delta\boldsymbol{u}}{\partial\xi^i}\cdot\boldsymbol{g}_j + \boldsymbol{g}_i\cdot\frac{\partial\delta\boldsymbol{u}}{\partial\xi^j}\big) \quad , \quad \delta\vec{E}_i = -\frac{\partial\delta\varphi}{\partial\xi^i} \quad . \tag{19}$$

The local Euler-Lagrange equations are obtained by integration by parts, consideration of Eq. (17) and the use of the divergence theorem in Eq. (18) as

$$(\boldsymbol{F}\widetilde{\boldsymbol{S}})\cdot\nabla_X+\boldsymbol{b}=\boldsymbol{0}\,,\quad \boldsymbol{E}-\bar{\boldsymbol{E}}=\boldsymbol{0}\,,\quad \frac{\partial W_0}{\partial\bar{\boldsymbol{E}}}-\widetilde{\boldsymbol{S}}=\boldsymbol{0}\qquad \text{in}\ \ \mathcal{B}_0 \tag{20}$$

$$\boldsymbol{F}\widetilde{\boldsymbol{S}}\cdot\boldsymbol{n}=\boldsymbol{t}\qquad \text{on}\ \ \partial_t\mathcal{B}_0 \tag{21}$$

$$\widetilde{\vec{\boldsymbol{D}}}\cdot\nabla_X-r=0\,,\quad \vec{\boldsymbol{E}}-\bar{\vec{\boldsymbol{E}}}=\boldsymbol{0}\,,\quad \frac{\partial W_0}{\partial\bar{\vec{\boldsymbol{E}}}}+\widetilde{\vec{\boldsymbol{D}}}=\boldsymbol{0}\qquad \text{in}\ \ \mathcal{B}_0 \tag{22}$$

$$\widetilde{\vec{\boldsymbol{D}}}\cdot\boldsymbol{n}=-q\qquad \text{on}\ \ \partial_q\mathcal{B}_0\quad , \tag{23}$$

where $\boldsymbol{n}$ is the outward normal vector on $\partial\mathcal{B}_0$ and the Nabla-operator ∇_X refers to the reference configuration. Eq. $(20)_1$ represents the equilibrium condition, Eq. $(20)_2$ is the geometrical field equation and Eq. $(20)_3$ describes the constitutive relation, whereas Eq. (21) ensures the boundary condition for a given traction on $\partial_t\mathcal{B}_0$. Eqs. (22) describe the charge conservation law, the field equation of the electric field and the constitutive relation, respectively. And finally Eq. (23) represents the boundary condition for a given surface charge q on $\partial_q\mathcal{B}_0$.

The weak form is with respect to the Green-Lagrangean strain measure nonlinear in the displacements and for more sophisticated materials the energy function W_0 is a nonlinear function of the gradient fields. To solve this equation iteratively within the finite element method the weak form is expanded in a Taylor series, which is truncated after the linear element $\delta\Pi^{k+1}=\delta\Pi^k+\mathrm{D}[\delta\Pi^k]\cdot(\Delta\boldsymbol{u},\,\Delta\varphi,\,\Delta\bar{\boldsymbol{\varepsilon}},\,\Delta\widetilde{\boldsymbol{\sigma}})\approx 0$. The superscript k denotes the iteration step. The linearization of the weak form results in

$$\begin{aligned}\mathrm{D}[\delta\Pi]\cdot(\Delta\boldsymbol{u},\,\Delta\varphi,\,\Delta\bar{\boldsymbol{\varepsilon}},\,\Delta\widetilde{\boldsymbol{\sigma}})=&\int_{\mathcal{B}_0}[\delta\bar{\boldsymbol{\varepsilon}}\cdot\frac{\partial\partial W_0}{\partial\bar{\boldsymbol{\varepsilon}}\,\partial\bar{\boldsymbol{\varepsilon}}}\Delta\bar{\boldsymbol{\varepsilon}}\ -\ \delta\bar{\boldsymbol{\varepsilon}}\cdot\Delta\widetilde{\boldsymbol{\sigma}}]\,\mathrm{d}V\\&+\int_{\mathcal{B}_0}[\delta\widetilde{\boldsymbol{\sigma}}\cdot\Delta\boldsymbol{\varepsilon}\ -\ \delta\widetilde{\boldsymbol{\sigma}}\cdot\Delta\bar{\boldsymbol{\varepsilon}}]\,\mathrm{d}V\\&+\int_{\mathcal{B}_0}[\delta\boldsymbol{\varepsilon}\cdot\Delta\widetilde{\boldsymbol{\sigma}}\ +\ \widetilde{\boldsymbol{\sigma}}\cdot\Delta\delta\boldsymbol{\varepsilon}]\,\mathrm{d}V\quad .\end{aligned} \tag{24}$$

Here ΔE_{ij} and $\Delta\vec{E}_i$ are defined similarly to Eq. (19) and $\Delta\delta\boldsymbol{\varepsilon}^T=[\Delta\delta\boldsymbol{E}^T,\,\boldsymbol{0}^T]$ with $\Delta\delta E_{ij}=\frac{1}{2}(\frac{\partial\delta\boldsymbol{u}}{\partial\xi^i}\cdot\frac{\partial\Delta\boldsymbol{u}}{\partial\xi^j}+\frac{\partial\Delta\boldsymbol{u}}{\partial\xi^i}\cdot\frac{\partial\delta\boldsymbol{u}}{\partial\xi^j})$. Furthermore it is noted that the

body force $\boldsymbol{b}$, the traction vector $\boldsymbol{t}$, the electric charge density r and the surface charge q are constant and not functions of the displacements.

Remark: If the conservation law of charge in material description is fulfilled one may show that

$$\int_{\mathcal{B}_0} -\vec{\boldsymbol{D}} \cdot \nabla_X + r \ \mathrm{d}V = \int_{\mathcal{B}_t} -\vec{\boldsymbol{d}} \cdot \nabla_x + r_t \ \mathrm{d}v = 0 \quad . \tag{25}$$

Here ∇_x refers to the deformed coordinates and $r_t = r \det \boldsymbol{F}$ is the charge density defined in the current configuration. For a detailed discussion see e.g. [36].

5 Finite element approximations

The finite element approximation is constructed by dividing the whole domain in element domains with $\mathcal{B} = \cup_{e=1}^{nelm} \mathcal{B}_e$, where $nelm$ is the total number of elements. By means of the isoparametric concept the geometry, the displacements and the electric potential are approximated on element level (index e) as

$$\boldsymbol{X}_e^h = \sum_{I=1}^{8} N_I \, \boldsymbol{X}_I \quad , \quad \boldsymbol{u}_e^h = \sum_{I=1}^{8} N_I \, \boldsymbol{u}_I \quad , \quad \varphi_e^h = \sum_{I=1}^{8} N_I \, \varphi_I \quad . \tag{26}$$

The superscript h is the characteristic size of the finite element discretization and indicates the finite element approximation. The quantities $\boldsymbol{X}_I$, $\boldsymbol{u}_I$ and φ_I are the position vector, the displacement vector and the electric potential at the node I. For a hexahedral element with eight nodes, see Fig. 1 the trilinear shape function at the node I is given as

$$N_I = \frac{1}{8}(1 + \xi_I^1 \xi^1)(1 + \xi_I^2 \xi^2)(1 + \xi_I^3 \xi^3) \quad \text{with} \quad -1 \leq \xi^i \leq +1 \tag{27}$$

and

$$\begin{aligned} \xi_I^1 &\in \{-1, \quad 1, \quad 1, -1, -1, \quad 1, \quad 1, -1\} \\ \xi_I^2 &\in \{-1, -1, \quad 1, \quad 1, -1, -1, \quad 1, \quad 1\} \\ \xi_I^3 &\in \{-1, -1, -1, -1, \quad 1, \quad 1, \quad 1, \quad 1\} \quad . \end{aligned} \tag{28}$$

Arranging N_I in the matrix $\boldsymbol{N} = [\boldsymbol{N}_1, \boldsymbol{N}_2, \boldsymbol{N}_3, \boldsymbol{N}_4, \boldsymbol{N}_5, \boldsymbol{N}_6, \boldsymbol{N}_7, \boldsymbol{N}_8]$ with $\boldsymbol{N}_I = \mathrm{diag}[N_I, N_I, N_I, N_I]$, the virtual displacements and the electric potential are interpolated as

$$\begin{bmatrix} \delta \boldsymbol{u}_e^h \\ \delta \phi_e^h \end{bmatrix} = \boldsymbol{N}\, \delta \boldsymbol{v}_e \quad , \tag{29}$$

where $\delta \boldsymbol{v}_e^T = [\delta \boldsymbol{v}_1^T, \delta \boldsymbol{v}_2^T, \ldots, \delta \boldsymbol{v}_8^T]$ is the virtual nodal vector with $\delta \boldsymbol{v}_I^T = [\delta u_1, \delta u_2, \delta u_3, \delta \varphi]_I^T$.

The Green-Lagrangean strain components Eq. (3) are defined by the covariant metric coefficients. The approximation of the covariant basis vectors is given as

$$\boldsymbol{G}_i^h = \sum_{I=1}^{8} N_{I,i}\, \boldsymbol{X}_I \quad , \quad \boldsymbol{g}_i^h = \sum_{I=1}^{8} N_{I,i}\, (\boldsymbol{X}_I + \boldsymbol{u}_I) \quad , \tag{30}$$

where $N_{I,i}$ is differentiated with respect to ξ^i. Accordingly the metric coefficients read

$$G_{ij}^h = \boldsymbol{G}_i^h \cdot \boldsymbol{G}_j^h \quad , \quad g_{ij}^h = \boldsymbol{g}_i^h \cdot \boldsymbol{g}_j^h \quad . \tag{31}$$

With the covariant basis vectors at hand one may establish the transformation matrices (4) and (8). For the approximation of the Green-Lagrangean strain components some assumed natural strain (ANS) interpolations are employed. To reduce transverse shear locking and to circumvent curvature thickness locking.

In accordance with [34] an ANS interpolation for the convective thickness strain is applied to overcome curvature thickness locking. The ANS interpolation considers four collocation points, which are defined in convective coordinates ξ^i as $i = (-1, -1, 0)$, $ii = (1, -1, 0)$, $iii = (1, 1, 0)$ and $iv = (-1, 1, 0)$. Considering eqs. (30), (31) the thickness strain is evaluated at these points and is interpolated bilinear through the element. Values evaluated at the collocation points are denoted with superscript $L = i, ii, iii, iv$, see Fig. 1.

To reduce the transverse shear locking in the case of distorted element geometries the ANS interpolations proposed in [33] are applied. Therefore the four collocation points $A = (-1, 0, 0)$, $B = (0, -1, 0)$, $C = (1, 0, 0)$, and $D = (0, 1, 0)$ are defined in convective coordinates ξ^i as depicted in Fig. 1. Employing eqs. (30), (31) the shear strains are evaluated at these points and denoted with the superscripts A, B, C and D, respectively.

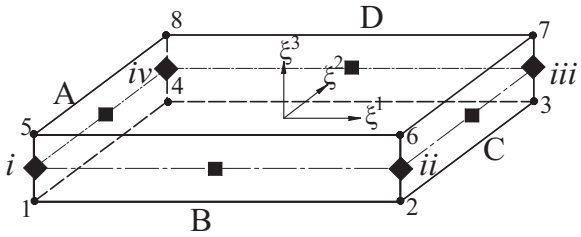

Figure 1: Collocation points of the different ANS-interpolations

Due to the ANS interpolations the brick element is not isotropic anymore. In particular, ξ^1, ξ^2 are now the in-plane coordinates and ξ^3 is the thickness coordinate of the present solid shell element. With respect to the ANS interpolations the approximation of the cartesian strain components read

$$\boldsymbol{E}_e^h = \boldsymbol{T}_S^{-T} \begin{bmatrix} \frac{1}{2}(g_{11}^h - G_{11}^h) \\ \frac{1}{2}(g_{22}^h - G_{22}^h) \\ \sum_{L=i}^{iv} \frac{1}{4}(1+\xi^{1\,L}\,\xi^1)(1+\xi^{2\,L}\,\xi^2)\,\frac{1}{2}(g_{33}^L - G_{33}^L) \\ (g_{12}^h - G_{12}^h) \\ (1-\xi^2)(g_{13}^B - G_{13}^B) + (1+\xi^2)(g_{13}^D - G_{13}^D) \\ (1-\xi^1)(g_{23}^A - G_{23}^A) + (1+\xi^1)(g_{23}^C - G_{23}^C) \end{bmatrix} \quad . \tag{32}$$

With respect to eqs. (7) and (9) the approximation of the electric field reads

$$\vec{\boldsymbol{E}}_e^h = -\sum_{I=1}^{8} \underbrace{\boldsymbol{J}^{-1} \begin{bmatrix} N_{I,1} \\ N_{I,2} \\ N_{I,3} \end{bmatrix}}_{\boldsymbol{B}_I^{\varphi} :=} \varphi_I \quad . \tag{33}$$

Introducing

$$\boldsymbol{B}_I^u = \boldsymbol{T}_S^{-T}$$
$$\begin{bmatrix} N_{I,1}\,\boldsymbol{g}_1^{hT} \\ N_{I,2}\,\boldsymbol{g}_2^{hT} \\ \sum_{L=i}^{iv}\ \frac{1}{4}(1+\xi^{1\,L}\,\xi^1)(1+\xi^{2\,L}\,\xi^2)\,N_{I,3}\,(\boldsymbol{g}_3^L)^T \\ N_{I,1}\,\boldsymbol{g}_2^{hT} + N_{I,2}\,\boldsymbol{g}_1^{hT} \\ (1-\xi^2)(N_{I,1}^B\,(\boldsymbol{g}_3^B)^T + N_{I,3}^B\,(\boldsymbol{g}_1^B)^T) + (1+\xi^2)(N_{I,1}^D\,(\boldsymbol{g}_3^D)^T + N_{I,3}^D\,(\boldsymbol{g}_1^D)^T) \\ (1-\xi^1)(N_{I,2}^A\,(\boldsymbol{g}_3^A)^T + N_{I,3}^A\,(\boldsymbol{g}_2^A)^T) + (1+\xi^1)(N_{I,2}^C\,(\boldsymbol{g}_3^C)^T + N_{I,3}^C\,(\boldsymbol{g}_2^C)^T) \end{bmatrix} \tag{34}$$

and

$$\boldsymbol{B} = [\boldsymbol{B}_1,\,\boldsymbol{B}_2,\,\boldsymbol{B}_3,\,\boldsymbol{B}_4,\,\boldsymbol{B}_5,\,\boldsymbol{B}_6,\,\boldsymbol{B}_7,\,\boldsymbol{B}_8] \quad \text{with} \quad \boldsymbol{B}_I = \begin{bmatrix} \boldsymbol{B}_I^u & \boldsymbol{0} \\ \boldsymbol{0} & \boldsymbol{B}_I^\varphi \end{bmatrix} \tag{35}$$

the virtual gradient fields are approximated by

$$\delta\boldsymbol{\varepsilon}_e^h = \boldsymbol{B}\,\delta\boldsymbol{v}_e \quad . \tag{36}$$

In the linearized weak form Eq. (24) the quantity $\widetilde{\boldsymbol{\sigma}}\cdot\Delta\delta\boldsymbol{\varepsilon}$ appears, which is approximated as

$$(\widetilde{\boldsymbol{\sigma}}\cdot\Delta\delta\boldsymbol{\varepsilon})^h = \delta\boldsymbol{v}_e^T\,\boldsymbol{G}\,\Delta\boldsymbol{v}_e \quad \text{with} \quad \boldsymbol{G} = \begin{bmatrix} \boldsymbol{G}_{11} & \boldsymbol{G}_{12} & \cdots & \boldsymbol{G}_{18} \\ \boldsymbol{G}_{21} & \boldsymbol{G}_{22} & \cdots & \boldsymbol{G}_{28} \\ \vdots & \vdots & \ddots & \vdots \\ \boldsymbol{G}_{81} & \boldsymbol{G}_{82} & \cdots & \boldsymbol{G}_{88} \end{bmatrix} \quad , \tag{37}$$

where $\boldsymbol{G}_{IJ}$ is defined for a node combination I and J as $\boldsymbol{G}_{IJ} = \mathrm{diag}[G_{IJ},\,G_{IJ},\,G_{IJ},\,0]$. Considering the ANS interpolations of [33] and [34] and the transformation matrix (5) the scalar G_{IJ} is obtained as

$$G_{IJ} = (\widetilde{\boldsymbol{S}}_e^h)^T\,\boldsymbol{T}_S^{-T}$$
$$\begin{bmatrix} N_{I,1}N_{J,1} \\ N_{I,2}N_{J,2} \\ \sum_{L=i}^{iv}\ \frac{1}{4}(1+\xi^{1\,L}\,\xi^1)(1+\xi^{2\,L}\,\xi^2)\,N_{I,3}N_{J,3} \\ N_{I,1}N_{J,2} + N_{I,2}N_{J,1} \\ \frac{1}{2}[(1-\xi^2)\,(N_{I,1}^B N_{J,3}^B + N_{I,3}^B N_{J,1}^B) + (1+\xi^2)\,(N_{I,1}^D N_{J,3}^D + N_{I,3}^D N_{J,1}^D)] \\ \frac{1}{2}[(1-\xi^1)\,(N_{I,2}^A N_{J,3}^A + N_{I,3}^A N_{J,2}^A) + (1+\xi^1)\,(N_{I,2}^C N_{J,3}^C + N_{I,3}^C N_{J,2}^C)] \end{bmatrix}, \tag{38}$$

where $\widetilde{\boldsymbol{S}}_e^h$ is the approximation of the stress field $\widetilde{\boldsymbol{S}}$ on element level.

5.1 Interpolation of the assumed strains and the electric field

The independent field $\bar{\boldsymbol{\varepsilon}}$ is interpolated by functions from the function space $\bar{\mathcal{E}}^h = [L_2(\mathcal{B}_0)]$, which leads to

$$\bar{\boldsymbol{\varepsilon}}_e^h = \boldsymbol{M}_\alpha\,\boldsymbol{\alpha} \quad \text{with} \quad \boldsymbol{M}_\alpha = \begin{bmatrix} \boldsymbol{N}_E & \boldsymbol{M}_E & \boldsymbol{0} & \boldsymbol{0} \\ \boldsymbol{0} & \boldsymbol{0} & \boldsymbol{N}_{\vec{E}} & \boldsymbol{M}_{\vec{E}} \end{bmatrix} \quad \text{and} \quad \boldsymbol{\alpha} \in \mathbb{R}^{40} \quad . \tag{39}$$

The matrices $\boldsymbol{N}_E$, $\boldsymbol{M}_E$, $\boldsymbol{N}_{\vec{E}}$, and $\boldsymbol{M}_{\vec{E}}$ are defined as

$$\boldsymbol{N}_E = \Bigg[\boldsymbol{T}_E^0,\, \boldsymbol{T}_E^0 \begin{bmatrix} \xi^3 & \xi^2\xi^3 & 0 & 0 & 0 \\ 0 & 0 & \xi^3 & \xi^1\xi^3 & 0 \\ 0 & 0 & 0 & 0 & 0 \\ 0 & 0 & 0 & 0 & \xi^3 \\ 0 & 0 & 0 & 0 & 0 \\ 0 & 0 & 0 & 0 & 0 \end{bmatrix}, \boldsymbol{T}_E \begin{bmatrix} \xi^2 & 0 & 0 & 0 & 0 & 0 & 0 \\ 0 & \xi^1 & 0 & 0 & 0 & 0 & 0 \\ 0 & 0 & \xi^1 & \xi^2 & \xi^1\xi^2 & 0 & 0 \\ 0 & 0 & 0 & 0 & 0 & 0 & 0 \\ 0 & 0 & 0 & 0 & 0 & \xi^2 & 0 \\ 0 & 0 & 0 & 0 & 0 & 0 & \xi^1 \end{bmatrix}\Bigg] \tag{40}$$

$$\boldsymbol{M}_E = \frac{\det \boldsymbol{J}^0}{\det \boldsymbol{J}} (\boldsymbol{T}_S^0)^{-T} \begin{bmatrix} \xi^1 & \xi^1\xi^2 & 0 & 0 & 0 & 0 & 0 \\ 0 & 0 & \xi^2 & \xi^1\xi^2 & 0 & 0 & 0 \\ 0 & 0 & 0 & 0 & \xi^3 & \xi^1\xi^3 & \xi^2\xi^3 \\ 0 & 0 & 0 & 0 & 0 & 0 & 0 \\ 0 & 0 & 0 & 0 & 0 & 0 & 0 \\ 0 & 0 & 0 & 0 & 0 & 0 & 0 \end{bmatrix} \quad , \tag{41}$$

$$\boldsymbol{N}_{\vec{E}} = (\boldsymbol{J}^0)^T \begin{bmatrix} 1 & 0 & 0 & \xi^2 & \xi^3 & \xi^2\xi^3 & 0 & 0 & 0 & 0 & 0 & 0 \\ 0 & 1 & 0 & 0 & 0 & 0 & \xi^1 & \xi^3 & \xi^1\xi^3 & 0 & 0 & 0 \\ 0 & 0 & 1 & 0 & 0 & 0 & 0 & 0 & 0 & \xi^1 & \xi^2 & \xi^1\xi^2 \end{bmatrix} \quad , \tag{42}$$

$$\boldsymbol{M}_{\vec{E}} = \frac{\det \boldsymbol{J}^0}{\det \boldsymbol{J}} \, (\boldsymbol{J}^0)^{-1} \begin{bmatrix} 0 & 0 & 0 \\ 0 & 0 & 0 \\ \xi^3 & \xi^1\xi^3 & \xi^2\xi^3 \end{bmatrix} \quad . \tag{43}$$

The transformation matrix $\boldsymbol{T}_E$ is obtained from Eq. (4) with $a = 1$ and $b = 2$ and $\boldsymbol{J}$ is defined by Eq. (8). The superscript 0 indicates that the quantities are evaluated at element center with $\xi^1 = \xi^2 = \xi^3 = 0$. It is noted that according to Eq. (43) the approximation of the electric field $\vec{E}$ is a bilinear function through the thickness. In Section 7.1.2 it is shown that this is necessary to satisfy the out of plane bending patch test.

It is remarked that the interpolation (41) is defined in the same manner as the interpolation of the enhanced assumed strain field proposed by Simo, Rifai [35]. Therefore we refer to that part of $\bar{\boldsymbol{E}}$ as enhanced assumed strain (EAS) field; for a more detailed discussion see [38]. Due to the fact that the interpolations of the assumed electric field are constructed in a similar way, we refer to the gradient field which is interpolated with Eq. (43) as enhanced assumed gradient (EAG) field.

5.2 Interpolation of the assumed stresses and dielectric displacements

Let $\widetilde{\mathcal{S}}^h = [L_2(\mathcal{B}_0)]$ be the approximation of the stress space $\widetilde{\mathcal{S}}$. The approximation of the assumed field $\widetilde{\boldsymbol{\sigma}}$ reads

$$\widetilde{\boldsymbol{\sigma}}_e^h = \boldsymbol{M}_\beta \, \boldsymbol{\beta} \quad \text{with} \quad \boldsymbol{M}_\beta = \begin{bmatrix} \boldsymbol{N}_S & \boldsymbol{0} \\ \boldsymbol{0} & \boldsymbol{N}_{\vec{D}} \end{bmatrix} \quad \text{and} \quad \boldsymbol{\beta} \in \mathbb{R}^{30} \quad . \tag{44}$$

The matrix $\boldsymbol{N}_S$ is given by Eq. (40), where instead of $\boldsymbol{T}_E^0$ and $\boldsymbol{T}_E$ the matrices $\boldsymbol{T}_S^0$ and $\boldsymbol{T}_S$, Eq. (5), are used. The matrix $\boldsymbol{N}_{\vec{D}}$ is identical to $\boldsymbol{N}_{\vec{E}}$ Eq. (42).

It is noted that the interpolation for the assumed stress field $\widetilde{\boldsymbol{S}}$ is similar to the interpolation which is used for hybrid stress brick elements based on the Hellinger-Reissner principle, see e.g. [39]. But in detail the formulations differ within the transformation strategy of the 18 independent parameters, see also [38].

5.3 Approximation of the weak form and its linearization

Considering the above interpolations in eqs. (18) and (24) one obtains the following matrices

$$\begin{aligned} \boldsymbol{A}_e &= \int_{\mathcal{B}_e} \boldsymbol{M}_\alpha^T \, \mathbb{D} \, \boldsymbol{M}_\alpha \, \mathrm{d}V_e & \boldsymbol{C}_e &= \int_{\mathcal{B}_e} \boldsymbol{M}_\alpha^T \, \boldsymbol{M}_\beta \, \mathrm{d}V_e \\ \boldsymbol{L}_e &= \int_{\mathcal{B}_e} \boldsymbol{B}^T \, \boldsymbol{M}_\beta \, \mathrm{d}V_e & \boldsymbol{K}_e &= \int_{\mathcal{B}_e} \boldsymbol{G} \, \mathrm{d}V_e \end{aligned} \tag{45}$$

and vectors

$$\begin{aligned} \boldsymbol{a}_e &= \int_{\mathcal{B}_e} \boldsymbol{M}_\alpha^T \, (\frac{\partial W_0}{\partial \bar{\boldsymbol{\varepsilon}}} - \widetilde{\boldsymbol{\sigma}}) \, \mathrm{d}V_e & \boldsymbol{b}_e &= \int_{\mathcal{B}_e} \boldsymbol{M}_\beta^T \, (\boldsymbol{\varepsilon} - \bar{\boldsymbol{\varepsilon}}) \, \mathrm{d}V_e \\ \boldsymbol{f}_e^{int} &= \int_{\mathcal{B}_e} \boldsymbol{B}^T \, \widetilde{\boldsymbol{\sigma}} \, \mathrm{d}V_e & \boldsymbol{f}_e^{ext} &= \int_{\mathcal{B}_e} \boldsymbol{N}^T \, \widetilde{\boldsymbol{p}} \, \mathrm{d}V_e + \int_{\partial\mathcal{B}_e} \boldsymbol{N}^T \, \widetilde{\boldsymbol{t}} \, \mathrm{d}A_e \, . \end{aligned} \tag{46}$$

on element level. In Eq. (46) the body and surface loads are determined by $\widetilde{\boldsymbol{p}}^T = [\boldsymbol{b}^T, r]$ and $\widetilde{\boldsymbol{t}}^T = [\boldsymbol{t}^T, q]$. With respect that Eq. (18) is solved iteratively with Newton's method the following approximation on element level is obtained as

$$\begin{aligned} &\big[\delta\Pi + \mathrm{D}[\delta\Pi] \cdot (\Delta\boldsymbol{u}, \, \Delta\varphi, \, \Delta\bar{\boldsymbol{\varepsilon}}, \, \Delta\widetilde{\boldsymbol{\sigma}})\big]_e^h \Rightarrow \\ &\begin{bmatrix} \delta\boldsymbol{v}_e \\ \delta\boldsymbol{\alpha}_e \\ \delta\boldsymbol{\beta}_e \end{bmatrix}^T \left(\begin{bmatrix} \boldsymbol{f}_e^{int} - \boldsymbol{f}_e^{ext} \\ \boldsymbol{a}_e \\ \boldsymbol{b}_e \end{bmatrix} + \begin{bmatrix} \boldsymbol{K}_e & \boldsymbol{0} & \boldsymbol{L}_e \\ \boldsymbol{0} & \boldsymbol{A}_e & -\boldsymbol{C}_e \\ \boldsymbol{L}_e^T & -\boldsymbol{C}_e^T & \boldsymbol{0} \end{bmatrix} \begin{bmatrix} \Delta\boldsymbol{v}_e \\ \Delta\boldsymbol{\alpha}_e \\ \Delta\boldsymbol{\beta}_e \end{bmatrix} \right) . \end{aligned} \tag{47}$$

Taking into account that the finite element interpolations for the fields $\bar{\boldsymbol{\varepsilon}}$, $\widetilde{\boldsymbol{\sigma}}$ do not require continuity across the element boundaries a condensation on element level yields the element stiffness matrix and the right hand side

$$\begin{aligned} \boldsymbol{K}_{Te} &= \boldsymbol{K}_e + \boldsymbol{L}_e \, (\boldsymbol{C}_e^T \, \boldsymbol{A}_e^{-1} \, \boldsymbol{C}_e)^{-1} \, \boldsymbol{L}_e^T \\ \boldsymbol{f}_e &= \boldsymbol{f}_e^{ext} - \boldsymbol{f}_e^{int} - \boldsymbol{L}_e \, (\boldsymbol{C}_e^T \, \boldsymbol{A}_e^{-1} \, \boldsymbol{C}_e)^{-1} (\boldsymbol{C}_e^T \, \boldsymbol{A}_e^{-1} \, \boldsymbol{a}_e + \boldsymbol{b}_e) \quad . \end{aligned} \tag{48}$$

After assembly over all elements $\boldsymbol{K}_T = \mathsf{A}_{e=1}^{nelm} \, \boldsymbol{K}_{Te}$, $\Delta\boldsymbol{v} = \mathsf{A}_{e=1}^{nelm} \, \Delta\boldsymbol{v}_e$ and $\boldsymbol{P} = \mathsf{A}_{e=1}^{nelm} \, \boldsymbol{f}_e$ one obtains

$$\boldsymbol{K}_T \, \Delta\boldsymbol{v} = \boldsymbol{P} \tag{49}$$

with the unknown incremental nodal displacements and the nodal values of the electric potential. It is remarked that the matrices $\boldsymbol{A}_e$ and $\boldsymbol{C}_e$ do not

change during the equilibrium iteration. The update of the internal degrees of freedoms reads

$$\begin{aligned} \Delta\boldsymbol{\beta}_e &= (\boldsymbol{C}_e^T\,\boldsymbol{A}_e^{-1}\,\boldsymbol{C}_e)^{-1}(\boldsymbol{L}_e^T\Delta\boldsymbol{v}_e + \boldsymbol{C}_e^T\,\boldsymbol{A}_e^{-1}\,\boldsymbol{a}_e + \boldsymbol{b}_e) \\ \Delta\boldsymbol{\alpha}_e &= \boldsymbol{A}_e^{-1}\,(\boldsymbol{C}_e\,\Delta\boldsymbol{\beta}_e - \boldsymbol{a}_e) \quad . \end{aligned} \tag{50}$$

6 Dynamic field problem and discrete approximation in time

In this Section the variational principle is extended for elastodynamic problems. It is noted that for the electric field quasi stationarity is assumed, which means that the change of the electric field in time t does not influence the field equations (22), (23). The change of the displacement vector $\boldsymbol{u}(t)$ is denoted as velocity $\dot{\boldsymbol{u}}(t)$ and the change of the velocity as acceleration $\ddot{\boldsymbol{u}}(t)$. Furthermore it is assumed that the body force $\boldsymbol{b}$ is now a function of time. In particular we define

$$\boldsymbol{b}(t) = \boldsymbol{b}_0 - d_0\,\dot{\boldsymbol{u}} - \rho_0\,\ddot{\boldsymbol{u}} \quad , \tag{51}$$

with $\boldsymbol{b}_0$ is the constant body force, d_0 denotes the damping constant and ρ_0 is the density with respect to the reference configuration. According to Eq. (51) the strong form of equilibrium reads $\mathrm{Div}(\boldsymbol{F}\boldsymbol{S})+\boldsymbol{b}_0-d_0\,\dot{\boldsymbol{u}}-\rho_0\,\ddot{\boldsymbol{u}}=\boldsymbol{0}$. The weak form in the dynamic case is then obtained as

$$\delta\pi(\boldsymbol{u},\,\varphi,\,\bar{\boldsymbol{\varepsilon}},\,\widetilde{\boldsymbol{\sigma}},\,\delta\boldsymbol{u},\,\delta\varphi) + \int_{\mathcal{B}_0} d_0\;\delta\boldsymbol{u}\cdot\dot{\boldsymbol{u}}\;\mathrm{d}\,V + \int_{\mathcal{B}_0} \rho_0\;\delta\boldsymbol{u}\cdot\ddot{\boldsymbol{u}}\;\mathrm{d}\,V = 0 \quad , \tag{52}$$

where in $\delta\pi$ Eq. (18) the body force $\boldsymbol{b}$ is substituted with $\boldsymbol{b}_0$. For the displacements, the velocity and the acceleration the initial boundary values have to be defined. The approximations of Eq. (52) is derived by introducing the interpolations

$$\dot{\boldsymbol{u}}_e^h = \bar{\boldsymbol{N}}\,\dot{\boldsymbol{v}}_e \quad \text{and} \quad \ddot{\boldsymbol{u}}_e^h = \bar{\boldsymbol{N}}\,\ddot{\boldsymbol{v}}_e \quad , \tag{53}$$

with $\bar{\boldsymbol{N}} = [\bar{\boldsymbol{N}}_1,\,\bar{\boldsymbol{N}}_2,\,\bar{\boldsymbol{N}}_3,\,\bar{\boldsymbol{N}}_4,\,\bar{\boldsymbol{N}}_5,\,\bar{\boldsymbol{N}}_6,\,\bar{\boldsymbol{N}}_7,\,\bar{\boldsymbol{N}}_8]$ and $\bar{\boldsymbol{N}}_I = \mathrm{diag}[N_I,\,N_I,\,N_I,\,0]$. Considering (53) in Eq. (52) yields the element damping matrix $\boldsymbol{D}_e$ and the consistent mass matrix $\boldsymbol{M}_e$ as

$$\boldsymbol{D}_e = \int_{\mathcal{B}_e} \bar{\boldsymbol{N}}^T d_0\;\bar{\boldsymbol{N}}\;\mathrm{d}\,V_e \quad , \quad \boldsymbol{M}_e = \int_{\mathcal{B}_e} \bar{\boldsymbol{N}}^T \rho_0\;\bar{\boldsymbol{N}}\;\mathrm{d}\,V_e \quad . \tag{54}$$

With respect to Eqs. (45), (46) the approximation of the weak form on element level reads

$$\begin{aligned}\delta\pi_e^h = \quad & \delta\boldsymbol{\alpha}_e^T\,[\boldsymbol{A}_e\,\boldsymbol{\alpha}_e - \boldsymbol{C}_e\,\boldsymbol{\beta}_e] \\ & + \delta\boldsymbol{\beta}_e^T\,[\int_{\mathcal{B}_e} \boldsymbol{M}_\beta^T\,\boldsymbol{\varepsilon}\;\mathrm{d}\,V_e - \boldsymbol{C}_e^T\,\boldsymbol{\alpha}_e] \\ & + \delta\boldsymbol{v}_e^T\,[\int_{\mathcal{B}_e} \boldsymbol{B}^T\,\widetilde{\boldsymbol{\sigma}}\;\mathrm{d}\,V_e - \boldsymbol{f}^{ext}] \;+\; \delta\boldsymbol{v}_e^T\,\boldsymbol{D}_e\dot{\boldsymbol{v}}_e \;+\; \delta\boldsymbol{v}_e^T\,\boldsymbol{M}_e\ddot{\boldsymbol{v}}_e \quad .\end{aligned} \tag{55}$$

Due to the fact that $\boldsymbol{\alpha}_e$, $\boldsymbol{\beta}_e$ do not require inter-element continuity, the first two terms in (55) are supposed to be zero on element level, which determines

$$\boldsymbol{\alpha}_e = \boldsymbol{A}_e^{-1}\,\boldsymbol{C}_e\,\boldsymbol{\beta}_e \quad , \quad \boldsymbol{\beta}_e = [\boldsymbol{C}_e^T\,\boldsymbol{A}_e^{-1}\,\boldsymbol{C}_e]^{-1}\int_{\mathcal{B}_e} \boldsymbol{M}_\beta^T\,\boldsymbol{\varepsilon}\;\mathrm{d}\,V_e \quad . \tag{56}$$

After assembling over all elements $\boldsymbol{F}^{int} = \mathsf{A}_{e=1}^{nelm}\,\boldsymbol{f}_e^{int}$, $\boldsymbol{F}^{ext} = \mathsf{A}_{e=1}^{nelm}\,\boldsymbol{f}_e^{ext}$, $\boldsymbol{M} = \mathsf{A}_{e=1}^{nelm}\,\boldsymbol{M}_e$ and $\boldsymbol{D} = \mathsf{A}_{e=1}^{nelm}\,\boldsymbol{D}_e$ the following residual vector is defined as

$$\boldsymbol{R} = \boldsymbol{F}^{int} - \boldsymbol{F}^{ext} + \boldsymbol{D}\dot{\boldsymbol{v}} + \boldsymbol{M}\ddot{\boldsymbol{v}} = \boldsymbol{0} \quad . \tag{57}$$

For the time integration the Newmark method with the standard parameters ($\beta = 0.25$, $\gamma = 0.5$) is employed.

7 Numerical Examples

The developed solid shell element formulation is implemented in a modified version of the program FEAP [40]. Some numerical examples are chosen to demonstrate the accurate behavior of the proposed element. Furthermore the examples demonstrate the ability of the present solid shell element to analyze piezoelectric devices.

In the first example the ability of the present element to pass relevant patch tests is discussed. Well established patch tests from structural mechanics are extended for piezoelectric structures. Here we consider the membrane patch test and the important out of plane bending patch tests. The fulfillment of the patch tests is essential to ensure convergence with respect to mesh refinement. It is shown that a linear interpolation of the electric field through the thickness is not sufficient to pass the patch tests. In the second example the robustness of the proposed element formulation with respect to mesh distortion is demonstrated. In the third example a piezoelectric

composite curved actuator is simulated. The results are compared to experimental data which confirms the applicability of the present element. The fourth example presents a curved piezoelectric structure within a dynamic analysis. A comparison with data from the literature verifies that the present element leads to correct results. Considering the geometrically nonlinear theory it is demonstrated that large displacement amplitudes arise in the case of vibration in eigenfrequency. Another geometrically nonlinear effect is the piezoelectric buckling of a plate, which is analyzed in the last example. An investigation of the post-buckling behavior yields that the piezoelectric buckling may be utilized for switching devices. The last example is concerned with an hemispherical shell subjected to an electrical load.

7.1 Patch tests

The patch tests are well known in structural mechanics, see e.g. [41]. Here, we adopt the classical mechanical patch tests and extend them to the piezoelectric finite element formulation. The test is fulfilled if the finite element formulation is able to reproduce constant stresses along with constant strains and a constant electric field for disturbed element geometries. In addition the piezoelectric element should be able to represent constant dielectric displacements. The patch tests are an important and necessary condition for convergence with respect to mesh refinement.

Furthermore we discuss the impact of the enhanced assumed gradient (EAG) interpolation (43) to the patch test. In detail three element formulations are considered, which differ in the interpolation Eq. (43) and are summarized in Tab. 1. The HSE-0 solid shell element has no enhanced assumed gradient for the electric field and therefore it is only possible to approximate an electric field, which is constant through the thickness. The element HSE-1 provides a linear interpolation whereas the present solid shell element HSE uses a bilinear interpolation through the thickness.

For shell structures it is distinguished between the membrane patch test and the out of plane bending patch test. In both tests we consider the element mesh illustrated in Fig. 2, which was introduced in [41]. The boundary conditions are chosen as follows: at $X_1 = 0$ all displacements are fixed and at $X_3 = -0.005$ the electric potential φ is set to zero. The system is subjected to different nodal forces F_u and F_l, which are described below. For the calculation of the two patch tests a geometrically linear behavior is assumed.

For the sake of simplicity and without loss of generality we assume a

solid shell element	HSE-0	HSE-1	HSE
EAG interpolation, $\boldsymbol{M}_{\vec{E}} =$	–	$\frac{\det \boldsymbol{J}^0}{\det \boldsymbol{J}} (\boldsymbol{J}^0)^{-1} \begin{bmatrix} 0 \\ 0 \\ \xi^3 \end{bmatrix}$	present solid shell, see Eq. (43)

Table 1: Applied element type and the enhanced assumed gradient interpolations

simplified piezoelectric material; the isotropic elastic material and the piezoelectric modulus are summarized in Tab. 2.

$E_1 = E_2 = E_3 = 123 \cdot 10^9\,\mathrm{N/m^2}$, $G_{12} = G_{13} = G_{23} = 61.5 \cdot 10^9\,\mathrm{N/m^2}$
$\mathrm{e}_{13} = -5\,\mathrm{C/m^2}$
$\epsilon = 12.5 \cdot 10^{-9}\,\mathrm{C/Nm^2}$

Table 2: Simplified material properties; not listed parameters are zero

7.1.1 Membrane patch tests

In this example we apply $F_u = F_l = 3 \cdot 10^4$ N, which produces a constant stress in X_1 direction as $S_{11} = 1 \cdot 10^8\,\mathrm{N/m^2}$. With respect to the above introduced material properties the problem is degenerated to a 1D problem, which is determined by two constitutive equations in X_1 direction

$$\begin{array}{rcrlcrll} 10^8\,\mathrm{N/m^2} & = & 123 \cdot 10^9 & \mathrm{N/m^2} & E_{11} & + & 5 & \mathrm{C/m^2}\ \vec{E}_3 \\ 0 & = & -5 & \mathrm{C/m^2} & E_{11} & + & 12.5 \cdot 10^{-9} & \mathrm{C^2/N\,m^2}\ \vec{E}_3 \end{array} \tag{58}$$

All other components of the stresses and dielectric displacements are equal to zero. From Eqs. (58) follows $E_{11} = 8 \cdot 10^{-4}$ and $\vec{E}_3 = 3.2 \cdot 10^5$ V/m and with respect to the boundary conditions the analytical solution for the displacements at $X_1 = 0.24$ m reads $u_1 = 1.92 \cdot 10^{-4}$ m, $u_2 = u_3 = 0$ and for the electric potential at the surface $X_3 = 0.005$ m it turns out $\varphi = 3.2 \cdot 10^3$ V. The results of a numerical solution of the problem with the above introduced elements are shown in Tab. 3. The stress and the dielectric displacement are calculated in a postprocess and are obtained as constant in the hole domain.

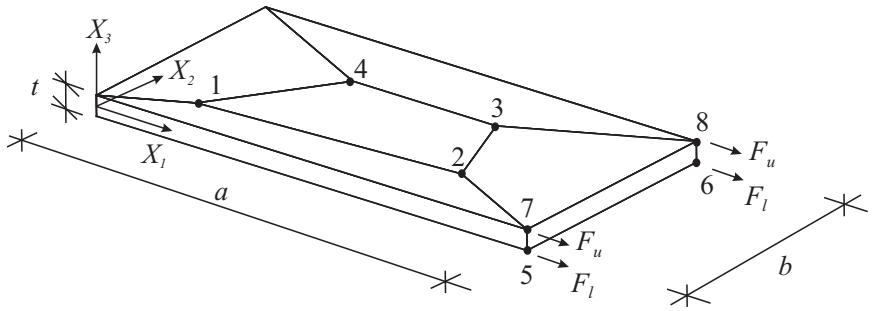

Geometry data:			Nodal coordinates: $(X_1,\ X_2,\ X_3)$			
a	=	0.24 m	1 :	(0.04,	0.02,	0.005)
b	=	0.12 m	2 :	(0.18,	0.03,	0.005)
t	=	0.01 m	3 :	(0.16,	0.08,	0.005)
			4 :	(0.08,	0.08,	0.005)

Figure 2: Element mesh for the patch tests and interior nodes 1, 2, 3, 4 on top of the surface

These results are in accordance with the analytical solution, which confirms that the membrane patch test is passed. It is noted that the enhanced assumed gradient interpolation Eq. (43) is not necessary to pass this test.

7.1.2 Out-of-plane bending patch test

The purpose of this test is to receive a constant bending stress. Therefore the system is subjected to the loads $F_u = -1 \cdot 10^5$ N and $F_l = +1 \cdot 10^5$ N, which results in a stress constant in X_1 direction and linear in X_3 $S_{11} = -2 \cdot 10^{11}\, X_3$ N/m^2. An analytical calculation yields a tip deflection $u_3 = 0.8\, X_1^2$ and an electric potential $\varphi = 0.32\, X_3^2 - 8 \cdot 10^{-6}$; evaluated at $X_1 = 0.24$ m and $X_3 = 0.005$ m yields

$$u_3 = 4.608 \cdot 10^{-2} \text{ m} \quad , \quad \varphi = 0 \text{ V} \quad . \tag{59}$$

It is noted that the analytical distribution of the electric potential is a quadratic function through the thickness. The reason therefore is that the applied couple force produces a linear stress distribution S_{11} through the thickness. With respect to the constitutive equations (58) and the material properties Tab. 2 it follows a linear strain distribution E_{11} and a linear

			HSE-0	HSE-1	HSE
		all nodes at			
u_1	[m]	$X_1 = 0.24$m	$1.92 \cdot 10^{-4}$	$1.92 \cdot 10^{-4}$	$1.92 \cdot 10^{-4}$
φ	[V]	$X_3 = 0.005$m	$3.20 \cdot 10^{-3}$	$3.20 \cdot 10^{-3}$	$3.20 \cdot 10^{-3}$
$\widetilde{S}_{11}$	[N/m^2]		$1 \cdot 10^8$	$1 \cdot 10^8$	$1 \cdot 10^8$
$\widetilde{\vec{D}}_1$	[C/m^2]		0	0	0

Table 3: Displacements, electric potential, stress and dielectric displacements calculated with different elements

electric field distribution $\vec{E}_3$ through the thickness. The electric potential is obtained by integrating the electric field considering the boundary conditions. It turns out that the electric potential is a quadratic function through the thickness, which is zero at the top and bottom surface. In Tab. 4 the displacement u_3 at the free edge of the plate and the electric potential at the top surface are shown.

		HSE-0	HSE-1	HSE
u_3 [m]	node 5	$4.68293 \cdot 10^{-2}$	$4.61156 \cdot 10^{-2}$	$4.60800 \cdot 10^{-2}$
	node 6	$4.68293 \cdot 10^{-2}$	$4.61394 \cdot 10^{-2}$	$4.60800 \cdot 10^{-2}$
	node 7	$4.68293 \cdot 10^{-2}$	$4.61156 \cdot 10^{-2}$	$4.60800 \cdot 10^{-2}$
	node 8	$4.68293 \cdot 10^{-2}$	$4.61394 \cdot 10^{-2}$	$4.60800 \cdot 10^{-2}$
φ [V]	nodes 1-4, 7, 8	≈ 0	≈ 0	≈ 0

Table 4: Displacements and electric potential calculated with different elements

It is found that only the HSE solid shell element provides correct results. The HSE-1 fails the out of plain patch test, it leads to wrong displacements, which are not even constant at the free edge. The HSE-0 without any EAG interpolations leads to a constant deflection, but this is larger than the analytical solution. This effect may be explained by considering the remaining interpolation matrix $\boldsymbol{N}_{\vec{E}}$ Eq. (42). It determines $\vec{E}_3$ as a bilinear function of ξ^1 and ξ^2 and constant in thickness direction ξ^3. Hence, it is not possible

		HSE-0	HSE	analytical solution
$\bar{E}_{11}$ [-]	nodes 5,6	$+0.813 \cdot 10^{-02}$	$+0.800 \cdot 10^{-02}$	$+0.800 \cdot 10^{-02}$
	nodes 7,8	$-0.813 \cdot 10^{-02}$	$-0.800 \cdot 10^{-02}$	$-0.800 \cdot 10^{-02}$
$\bar{\vec{E}}_3$ [V/m]	nodes 5,6	≈ 0	$-0.320 \cdot 10^{+07}$	$-0.320 \cdot 10^{+07}$
	nodes 7,8	≈ 0	$+0.320 \cdot 10^{+07}$	$+0.320 \cdot 10^{+07}$

Table 5: Numerical and analytical solutions for the strain E_{11} and the electric field $\vec{E}_3$

to approximate a linear distribution of $\bar{\vec{E}}_3$ through the thickness. As a result the electric field is approximated as zero, see Tab. 5. Consequently the strain $\bar{E}_{11}$ is overestimated to obtain the linear stress distribution S_{11}, which leads to the pure mechanical solution without any piezoelectric coupling.

7.2 Bimorph

This is another geometrically linear example, which is employed to investigate the sensitivity of the present element with respect to mesh distortions. The cantilever beam with its geometrical data is depicted in Fig. 3. The beam structure is formed by two piezoelectric layers. The layers are glued together, where the polarized directions are opposite in X_3 direction.

Here we consider the finite element mesh introduced by Sze et al. [17], where the mesh distortion is described by the parameter s. The system is loaded by a unit Voltage through the thickness, which produces a constant electric field of $\vec{E}_3 = 10^3$ V/m. An analytical solution is proposed by Tzou [42], who considered an Euler-Bernoulli beam theory. To assess the element accuracy by the beam solution, the Poisson's ratio is set to zero. The material data are summarized in Tab. 6.

Due to the fact the piezoelectric layers are polarized in opposite directions the applied electric field induces in one layer a tension stress and in the other layer a compression stress. In other words the applied constant electric field produces a bending behavior of the bimorph beam. In Tab. 7 the analytical tip deflection w of the cantilever is compared to the numerical results, which are computed with the present solid shell element for different distortion parameters s. It is noted that the solutions agree exactly, even for a highly

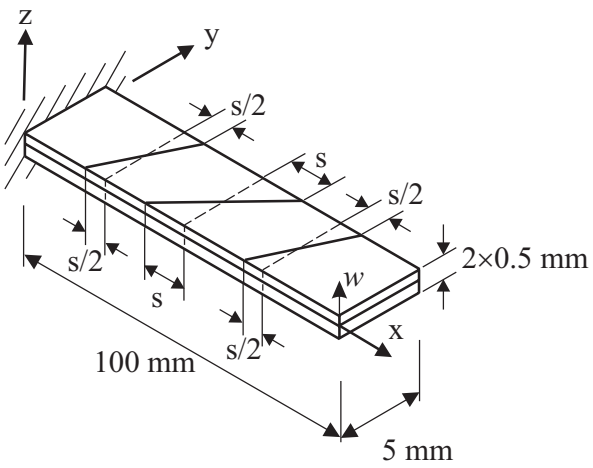

Figure 3: The finite element model of a bimorph cantilever

$E_1 = E_2 = E_3 = 2 \cdot 10^9\,\mathrm{N/m^2}$, $G_{12} = G_{13} = G_{23} = 1 \cdot 10^9\,\mathrm{N/m^2}$
$\mathrm{e}_{13} = 0.046\,\mathrm{C/m^2}$
$\epsilon = 0.1062 \cdot 10^{-9}\,\mathrm{C/Nm^2}$

Table 6: Material data of piezoelectric PVDF (Polyvinylidene-Fluoride); not listed parameters are zero

distorted mesh s = 50, in which all elements appear as triangles, see Fig. 4. For the sensitivity of the element with respect to mechanical loading and mesh distortion see [38].

analytical solution Tzou [42]	numerical solution present element	
w	s	w
$0.345\,\mu\mathrm{m}$	$1 - 50$	$0.345\,\mu\mathrm{m}$

Table 7: Analytical and numerical tip displacements w

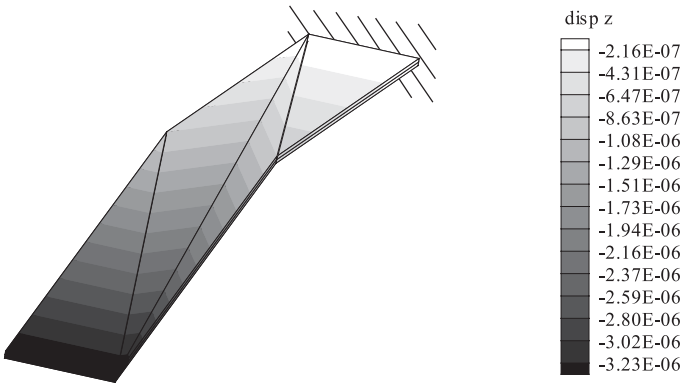

Figure 4: Deformed finite element model for $s = 50$ with a plot of the vertical displacement distribution in [m]

7.3 Curved piezoelectric composite actuator

In this example a lightweight piezoelectric composite curved actuator (LIPCA) is analyzed with the proposed geometrically nonlinear solid shell element; the results are compared to experimental data published in [43]. LIPCAs are manufactured as composites with different layers depending on the type of the LIPCA. The layup of the LIPCA-C1 is presented in e.g. [44, 45] and consists out of four layers: two Glass/Epoxy layers, one PZT Ceramic, and one Carbon/Epoxy layer. The stacked layers are vacuum bagged which results in an initial curvature. The cross section of the composite with the layup is depicted in Fig. 5. The curved structure and the geometrical data are shown in Fig. 6. The material data for the two epoxy materials and the material properties of the PZT-5A piezoelectric ceramic, see [43], are listed in Tab. 8; values in thickness direction are assumed.

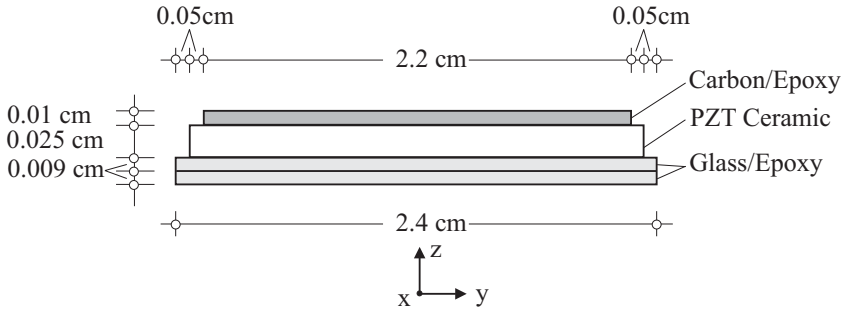

Figure 5: Cross section of LIPCA-C1

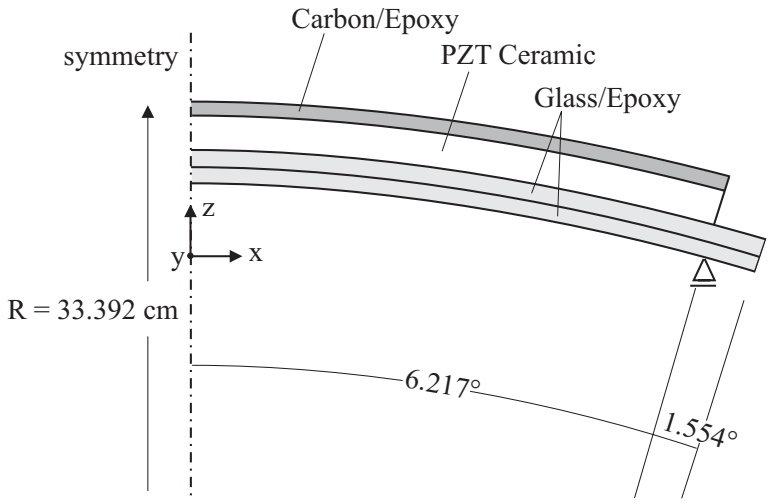

Figure 6: Curved structure of LIPCA-C1

Carbon/Epoxy
$E_1 = 231.2 \cdot 10^9\,\mathrm{N/m^2}$, $E_2 = E_3 = 7.2 \cdot 10^9\,\mathrm{N/m^2}$
$\nu_{12} = \nu_{13} = 0.29$, $\nu_{23} = 0.32$
$G_{12} = G_{13} = 4.3 \cdot 10^9\,\mathrm{N/m^2}$, $G_{23} = 2.15 \cdot 10^9\,\mathrm{N/m^2}$
$\rho = 1510\,\mathrm{kg/m^3}$
Glass/Epoxy
$E_1 = E_2 = 21.7 \cdot 10^9\,\mathrm{N/m^2}$, $E_3 = 0.217 \cdot 10^9\,\mathrm{N/m^2}$
$\nu_{12} = 0.13$, $\nu_{13} = \nu_{23} = 0.013$
$G_{12} = 3.99 \cdot 10^9\,\mathrm{N/m^2}$, $G_{23} = G_{13} = 0.399 \cdot 10^9\,\mathrm{N/m^2}$
$\rho = 1910\,\mathrm{kg/m^3}$
PZT Ceramic
$E_1 = E_2 = E_3 = 67 \cdot 10^9\,\mathrm{N/m^2}$
$\nu_{12} = \nu_{13} = \nu_{23} = 0.31$
$G_{12} = G_{13} = G_{23} = 25.57 \cdot 10^9\,\mathrm{N/m^2}$
$\mathrm{e}_{13} = \mathrm{e}_{23} = -9.30032142\,\mathrm{C/m^2}$, $\mathrm{e}_{33} = 20.3638\,\mathrm{C/m^2}$,
$\mathrm{e}_{51} = \mathrm{e}_{62} = 14.5749\,\mathrm{C/m^2}$
$\epsilon = 15.31742 \cdot 10^{-9}\,\mathrm{C^2/N\ m^2}$
$\rho = 7800\,\mathrm{kg/m^3}$

Table 8: Material properties and density ρ of the employed layers

According to Yoon et al. [43] the experimental setup is designed to simulate a simply supported boundary condition, which is shown in Fig. 6. The actuator is loaded by applying a power supply of ±50, ±100, ±150 and ±200 (400 Vpp; Volt peak to peak) at an operating frequency of 1.0 Hz. Yoon et al. [43] measured the vertical displacement amplitude in z direction at the center point of the actuator for each applied electric field.

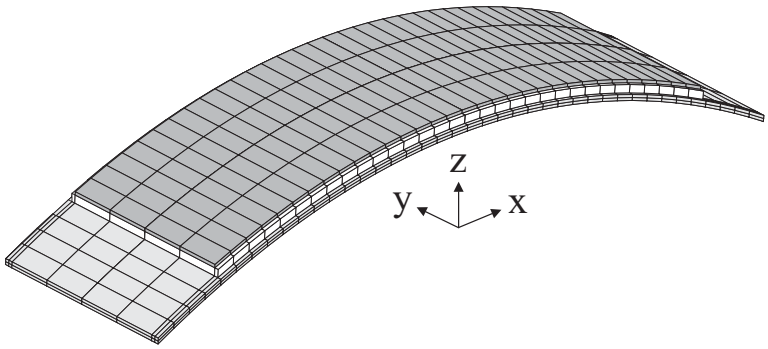

Figure 7: Finite element model of the LIPCA-C1

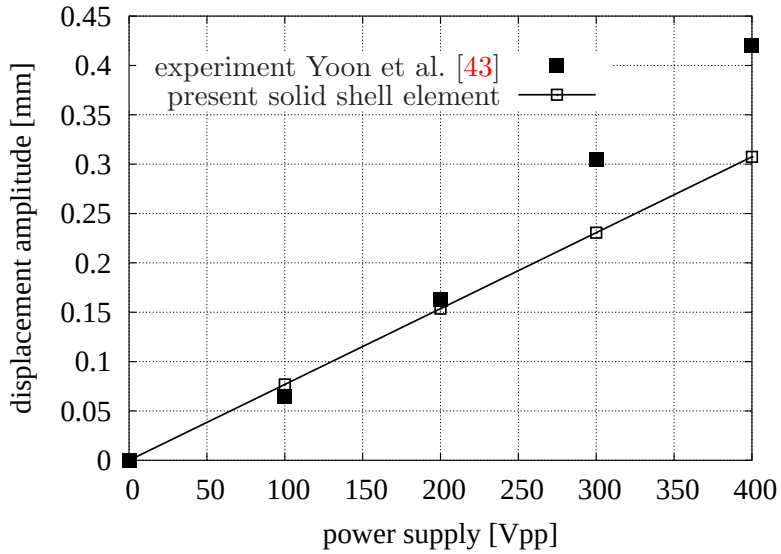

Figure 8: Excitation deflection diagram

The LIPCA-C1 was modeled with 960 solid shell elements, see Fig. 7. A further mesh refinement does not change the displacement response significantly. The displacement amplitudes for the different excitations are depicted in Fig. 8. For loadings smaller or equal than 200 Vpp the numerical solution agrees very well with the experimental data. For a loading larger than 200 Vpp a nonlinear displacement response of the experimental data is observed. Yoon et al. noted that a nonlinear finite element analysis seems

to be required to predict the nonlinear behavior. Due to the fact that the present solid shell formulation considers geometrical nonlinearities, the displacement response of the experimental data must be caused by some other nonlinearities or modeling differences.

7.4 Semicircular ring shell

The semicircular ring shell is a popular example for the dynamic analysis of piezoelectric curved structures and may be found in [19, 17, 15]. In the geometrically linear case the presented element verifies well known results form the literature. The geometrically non-linear case demonstrates that the present element is in contrast to the above cited formulations able to handle large deformations.

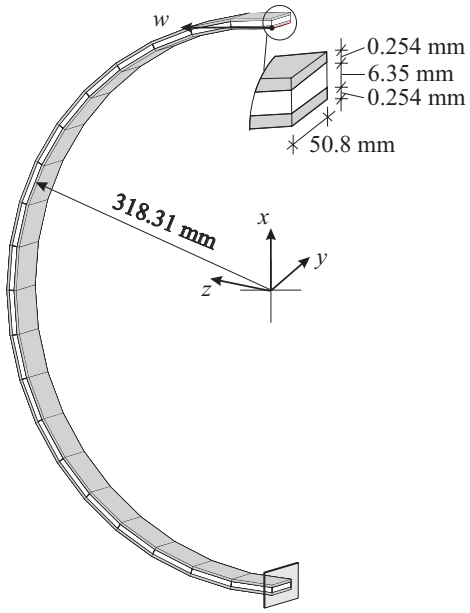

Figure 9: Geometry and finite element model of the semicircular ring

The composite structure of the ring shell consists of an inner piezoelectric sensor layer, a steel ring and a piezoelectric layer at the outside, which serves as actuator. The geometrical data are presented in Fig. 9 and the material data are summarized in Tab. 9. Here the marked radius regards to the inner

Steel
$E_1 = E_2 = E_3 = 68.95 \cdot 10^9\,\mathrm{N/m^2}$
$\nu_{12} = \nu_{13} = \nu_{23} = 0.3$
$G_{12} = G_{13} = G_{23} = E_1/(2(1+\nu_{12}))$
$\rho = 7750\,\mathrm{kg/m^3}$
PZT
$E_1 = E_2 = E_3 = 63 \cdot 10^9\,\mathrm{N/m^2}$
$\nu_{12} = \nu_{13} = \nu_{23} = 0.3$
$G_{12} = G_{13} = G_{23} = E_1/(2(1+\nu_{12}))$
$\mathrm{e}_{13} = \mathrm{e}_{23} = 21.677\,\mathrm{C/m^2}$, $\mathrm{e}_{33} = 12.955\,\mathrm{C/m^2}$
$\epsilon = 16.5 \cdot 10^{-9}\,\mathrm{C^2/N\ m^2}$
$\rho = 7600\,\mathrm{kg/m^3}$

Table 9: Material constants for the semicircular ring, see Sze et al.[17]; not listed parameters are zero

edge of the steel ring. The semicircular ring is modeled by 3 elements through the thickness (one element for each layer) and 1 element through the width. The number of elements in circumferential direction varies and is defined below.

The lowest eigenfrequencies of the steel ring in the absence of the piezoelectric layers are listed in Tab. 10. The eigenfrequencies $f_i = \omega_i/(2\pi)$ are calculated by solving the problem $(\boldsymbol{K} - \omega_i \boldsymbol{M})\boldsymbol{\phi} = \boldsymbol{0}$, where $\boldsymbol{K}$ is the geometrically linear stiffness matrix. The calculated eigenvalues of the present element verify the results of [17].

element formulation	element mesh width×circum.×thickn.	f_1	f_2	f_3
Sze et al. [17]	$1 \times 10 \times 1$	3.6822	5.8278	11.838
	$2 \times 20 \times 1$	3.6810	5.8041	11.691
present	$1 \times 10 \times 1$	3.6832	5.8352	11.843
	$1 \times 20 \times 1$	3.6727	5.8071	11.660

Table 10: Eigenfrequencies of the steel ring

For the dynamic analysis the ring shell with the PZT layers is stimulate to oscillate in the first eigen-mode. Here an active control model is applied to control the amplitude. Within this model the voltage of the inner PZT layers are taken to be the input of the controllers which actuate the outer PZT layer opposite to the inner layer. The active control algorithm is summarized in the App. The controller gain is set to $\boldsymbol{T}_{\varphi} = 0.2088\,\mathbf{1}\,\mathrm{s}$ and the passive damping is assumed to be $d = 0.0002\,\mathrm{kg/s}$. For this example the piezoelectric layers cover only the half steel ring in circumferential direction. An initial deformation is applied to the ring, which is exactly the scaled first eigen-mode with a tip deflection of 4 cm. The semicircular ring is modeled by 40 elements in circumferential direction. For the time integration a modified Newmark's method is employed. The HHT-method, see [46], handles the numerical dissipation much better. Within this method the numerical damping is controlled by the parameter $\alpha = 0.05$. The calculations are performed with a time step size of $2 \cdot 10^{-2}\,\mathrm{s}$. Fig. 10 shows the tip displacement versus time. For this geometrically linear example the comparison with Sze et al.[17] confirms a good agreement. In [17] the electric field in thickness direction is approximated as constant, whereas in the present element the electric field is approximated as a bilinear function in thickness direction, which is necessary to pass the out of plane bending patch test. However, it seems to have only a minor influence to this example.

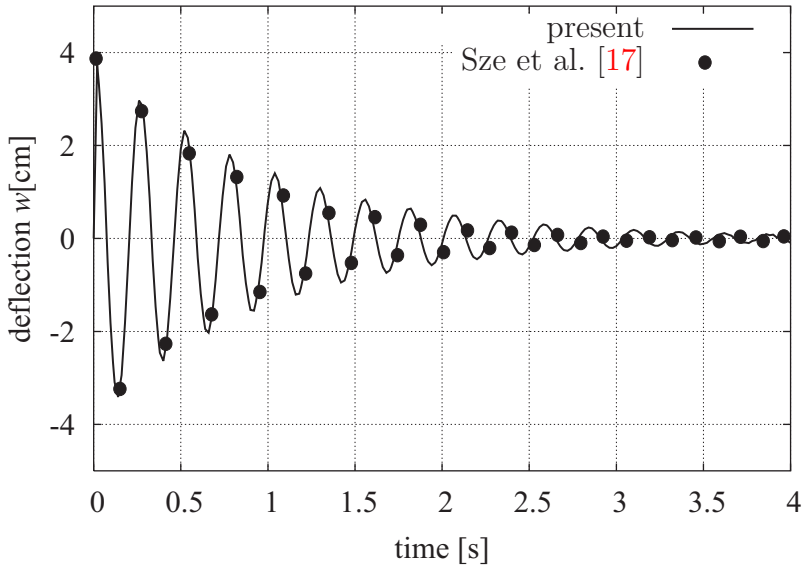

Figure 10: Controlled vibration of the ring

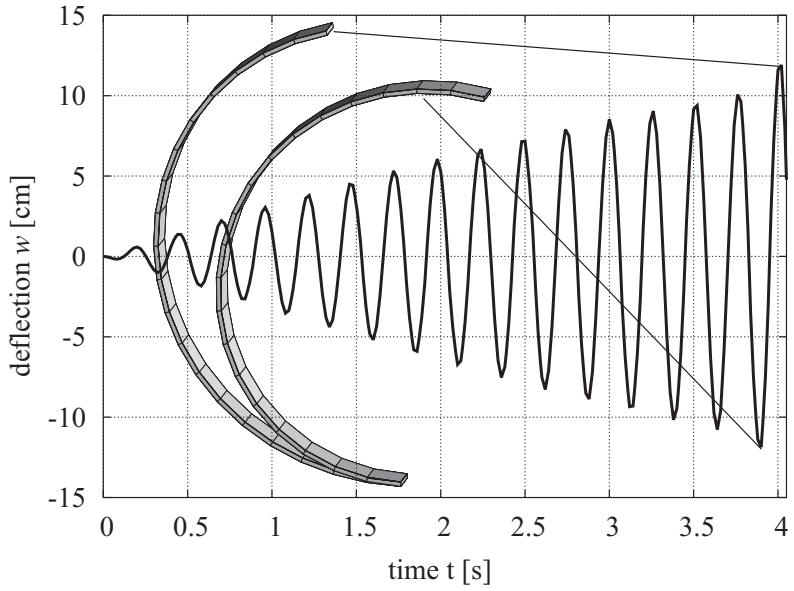

Figure 11: Stimulated vibration of the ring with deformed configurations

In contrast to [19, 17, 15] the present element is not restricted to geometrically linear examples. To produce large deflections the actuator (the outer PZT layer) is loaded by an electric potential $\varphi(t) = 450\, cos(2\,\pi\, f_1\, t)$ at the outside, where f_1 is the lowest eigenfrequency. At the inside of the actuator and the sensor the electric potential is set equals to zero. Within this example the piezoelectric layers cover the whole ring shell, which is modeled by 20 elements in circumferential direction. In Fig. 11 the displacement versus time is plotted and the deformed configurations are shown. The calculation is performed with Newmark's method and a time step size of $2 \cdot 10^{-2}$ s.

7.5 Piezoelectric buckling

In this example the buckling behavior of a piezoelectric plate is analyzed. Two load cases are considered a mechanical loading by a force and an electrical loading by an electric potential. To check the finite element model the numerical results are compared with analytical solutions for mechanical buckling. In the case of buckling induced by the electric field the numerical results are compared with those proposed in [26]. A square plate consisting out of six layers is considered; the layup and the geometrical data of the plate are given in Fig. 12. The principal directions of the graphite epoxy plies lie in the X_1-X_2 plane, where the angle is defined with respect to the X_1 axes, see Fig. 12. The plate is modeled by 16×16 elements in-plane and 6 elements through the thickness.

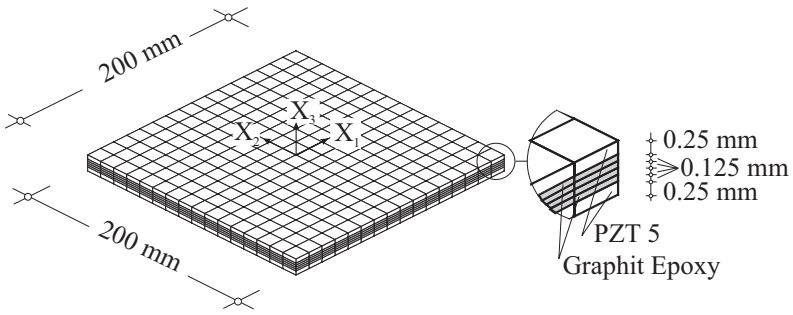

Figure 12: Finite element model of the laminated square plate with the stacking sequence of Graphite Epoxy $[0^o, 90^o, 90^o, 0^o]$

According to [26] the material data is summarized in Tab. 11. Due to the

fact that the material constants in thickness direction are not required in the plate formulation of [26], they are assumed in the present work.

Graphite Epoxy 0^o
$E_1 = E_2 = 132.4 \cdot 10^9\,\mathrm{N/m^2}$, $E_3 = 10.8 \cdot 10^9\,\mathrm{N/m^2}$
$\nu_{12} = \nu_{13} = 0.24$, $\nu_{23} = 0.49$
$G_{12} = G_{13} = 5.6 \cdot 10^9\,\mathrm{N/m^2}$, $G_{23} = 3.6 \cdot 10^9\,\mathrm{N/m^2}$
PZT-5 ceramic
$E_1 = 62.0 \cdot 10^9\,\mathrm{N/m^2}$, $E_2 = E_3 = 54.9 \cdot 10^9\,\mathrm{N/m^2}$
$\nu_{12} = \nu_{13} = \nu_{23} = 0.31$
$G_{12} = G_{13} = 23.6 \cdot 10^9\,\mathrm{N/m^2}$, $G_{23} = 18.0 \cdot 10^9\,\mathrm{N/m^2}$
$\mathbb{e}_{13} = \mathbb{e}_{23} = -12.006\,\mathrm{C/m^2}$, $\mathbb{e}_{33} = 17.277\,\mathrm{C/m^2}$, $\mathbb{e}_{51} = \mathbb{e}_{62} = 15.812\,\mathrm{C/m^2}$
$\epsilon = 22.99 \cdot 10^{-9}\,\mathrm{C^2/N\ m^2}$

Table 11: Material properties of the plate

The two load cases are depicted in Fig. 13. The mechanical load n_x is applied only in X_1 direction, where the plate is simply supported at the boundary in X_3 direction. For the electrical loading an electric potential is applied to the upper and lower surface of the piezoelectric layers; where all three displacements of the middle surface at the boundary of the plate are fixed, see Fig. 13.

Two different electric conditions are considered for the mechanical loading n_x. For the closed circuit (CC) the electric condition $0\,V$ is applied to the top and bottom electrodes of each piezoelectric layer. For the open circuit (OC) the electric condition reads: the inner electrodes are grounded while the outer electrodes remain free. In Tab. 12 the critical loads n_x for the first four buckling modes are listed and are compared with numerical results obtained in [26] and with analytical solutions of [47].

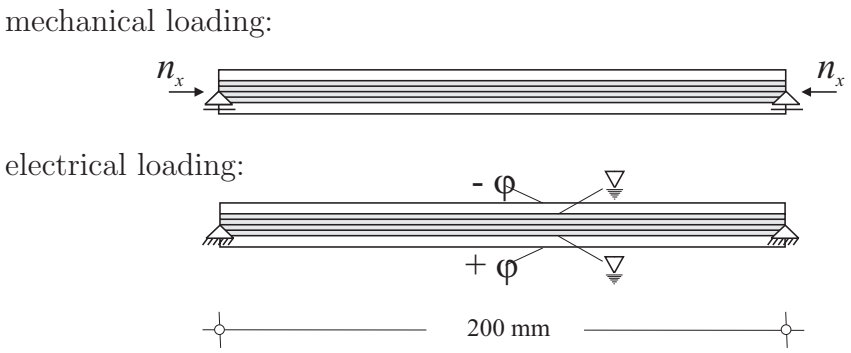

Figure 13: The two loading cases and the boundary conditions

	present solid shell element		Varelis, Saravanos [26]		elastic analytical solution [47]
order	CC	OC	CC	OC	
1	5.38	6.38	5.33	7.22	5.37
2	9.15	10.71	8.98	11.94	9.00
3	17.31	20.13	16.50	21.80	16.50
4	21.82	25.80	26.70	35.60	27.20

Table 12: Stability load n_x [N/m] for the first four buckling modes

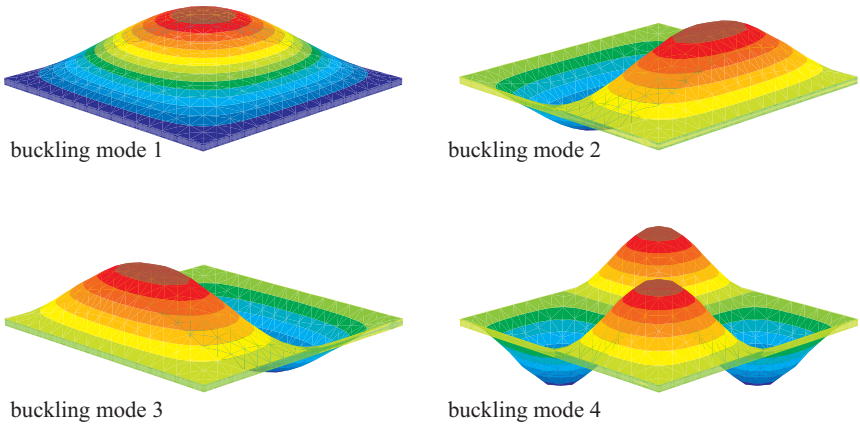

Figure 14: First four piezoelectric bucking modes with a plot of the normalized u_3 displacement

The results agree very well for the first three buckling loads, the slightly differences may be explained by the differences of the underlying formulations. The purely elastic analytical solution is based on the classical laminate plate theory. Also for the formulation proposed by Varelis and Saravanos constant shear strains through the thickness are assumed, whereas the present formulation allows different transverse shear strains for each layer. Furthermore, Varelis and Saravanos assumed a constant electric field for each piezoelectric layer which stands in contrast to the present work, in which a linear distribution is allowed. The latter argument may be the reason for the differences occurring for the fourth buckling mode in case of the OC electric condition.

Piezoelectric buckling is observed by increasing the electric potential up to a critical value. With respect to the coupling matrix, see Tab 11, an increasing negative electric field leads to negative values for the stresses in X_1 and X_2 directions, which cause a loss of stiffness. The first four buckling modes are calculated with the present solid shell element and are shown in Fig. 14. The corresponding critical values of φ are listed in Tab. 13. The good agreement of the critical electric potentials confirms that the present solid shell element performs well within a piezoelectric buckling analysis.

	present solid shell element	Varelis, Saravanos [26]
order		
1	70.58	68.8
2	172.47	170.5
3	193.26	189.4
4	286.07	289.3

Table 13: Critical electric potential φ [V] for the first four buckling modes

The work of [26] is restricted to calculate the critical loads and buckling modes. With the present formulation the post buckling behavior is analyzed. This is important if the piezoelectric plate is employed as a switch device. Here we introduce such a device by modifying the geometry of the considered plate slightly as shown in Fig. 15. The geometrical imperfection initializes the buckling direction, thus the stability problem becomes a pure bending

problem.

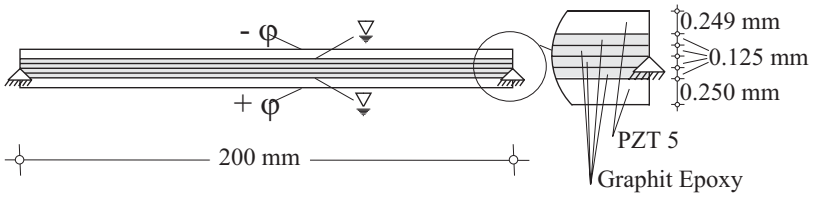

Figure 15: Modified geometry of the piezoelectric plate with the stacking sequence of Graphite Epoxy $[0^o, 90^o, 90^o, 0^o]$

In Fig. 16 the electric potential ϕ is plotted versus the vertical deflection at the center point of the plate. An increasing load from $\varphi = 60$ V to $\varphi = 120$ V leads to a large change in the center deflection $u_3 = 0.002$ mm to $u_3 = 0.731$ mm. This effect may be utilized for a switching device. In Fig. 17, 18 the stress and dielectric displacement distribution for the loading $\varphi = 200$ V are depicted.

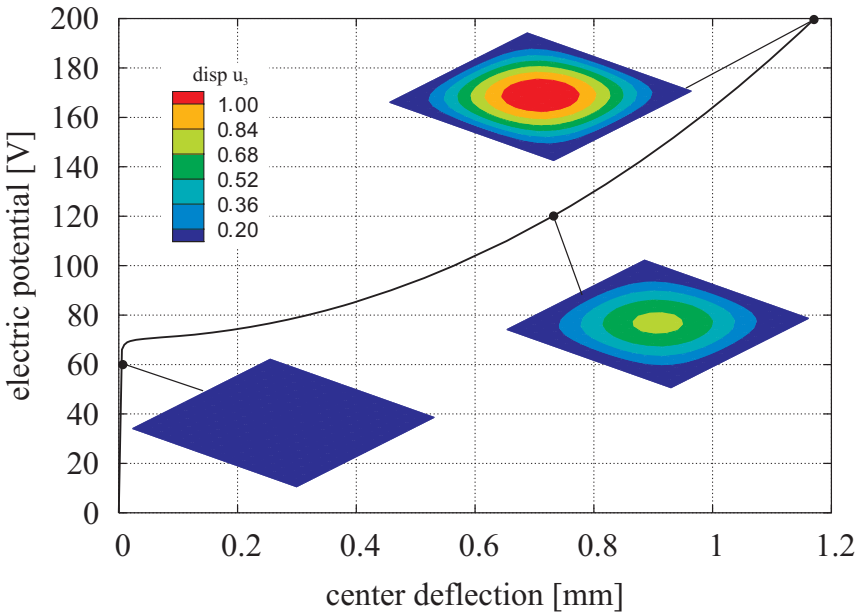

Figure 16: Load deflection curve and plots of the vertical deflection at characteristic points

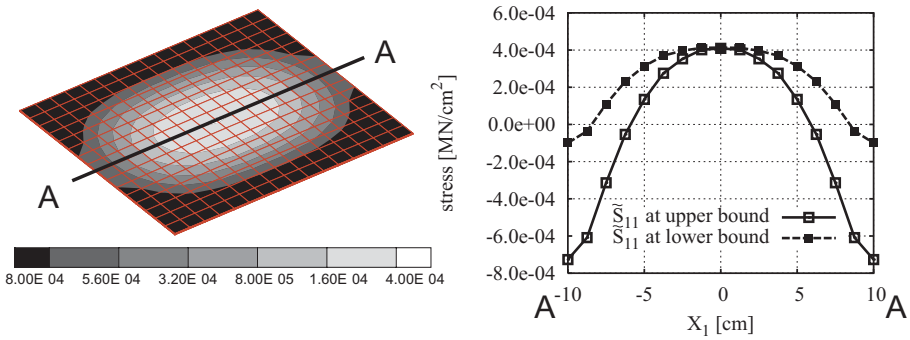

Figure 17: Stress $\tilde{S}_{11}$ at $\varphi = 200$ V; left: the stress plot at the upper surface; right: the stress distribution of the upper piezoelectric layer at the upper and lower bound

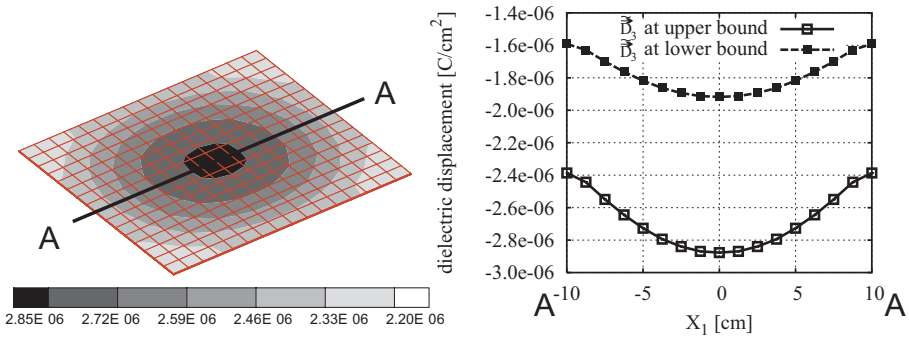

Figure 18: Dielectric displacement $\tilde{\tilde{D}}_3$ at $\varphi = 200$ V; left: the plot at the upper surface; right: the dielectric displacement distribution of the upper piezoelectric layer at the upper and lower bound

7.6 Hemispherical shell with an 18^o hole

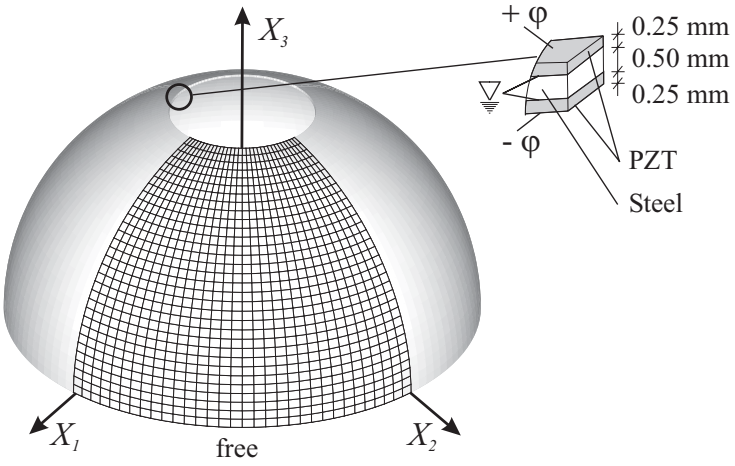

Figure 19: System and layup of the hemispherical shell with 18^o degree hole

The last example is concerned with a double curved shell structure. The hemispherical shell with an 18^o hole has an inner radius of 10 cm and is

depicted in Fig. 19. With respect to symmetry only a quarter of the shell is modeled by 32 by 32 finite elements in plane and 3 elements through the thickness. The edge of the hole is fixed in X_3-direction. The system is loaded by applying an electric potential $\varphi = 500\,\mathrm{V}$ at the inner and outer surface of the piezoelectric layers, see Fig. 19.

Steel
$E_1 = E_2 = E_3 = 21.0 \cdot 10^{10}\,\mathrm{N/m^2}$
$\nu_{12} = \nu_{13} = \nu_{23} = 0.3$
PZT-4 ceramic
$E_1 = E_2 = E_3 = 81.3 \cdot 10^{9}\,\mathrm{N/m^2}$
$\nu_{12} = \nu_{13} = \nu_{23} = 0.33$
$\mathrm{e}_{13} = \mathrm{e}_{23} = -5.20279\,\mathrm{C/m^2}$, $\mathrm{e}_{33} = 15.08041\,\mathrm{C/m^2}$, $\mathrm{e}_{51} = \mathrm{e}_{62} = 12.71794\,\mathrm{C/m^2}$
$\epsilon = 6.75154 \cdot 10^{-9}\,\mathrm{C^2/N\ m^2}$

Table 14: Material properties of the plate

The material properties are defined with respect to the orthonormal basis system $\boldsymbol{t}_i$, which was introduced in Section 2. Here, $\boldsymbol{t}_1$ acts in meridian direction, $\boldsymbol{t}_2$ in circumferential direction and $\boldsymbol{t}_3$ in normal outward direction. The material data are listed in Tab. 14.

A nonlinear calculation yields an radial displacement of the lower inner edge of $12.51\,\mu$m and a deflection in X_3 direction of $-2.43\,\mu$m. Due to the loading conditions it is expected that the inner piezoelectric layer is expanded and the outer piezoelectric layer shrinks. This leads to a roll up effect of the lower edge of the hemispherical shell. The deformed structure is shown in Fig. 20.

8 Conclusion

In this paper a geometrically nonlinear solid shell element to analyze piezoelectric structures is presented. The finite element formulation is based on the variational principle of Hu-Washizu and includes six independent field variables. The mixed formulation fulfills the electric charge conservation law exactly. A complete geometrically nonlinear theory is presented, which al-

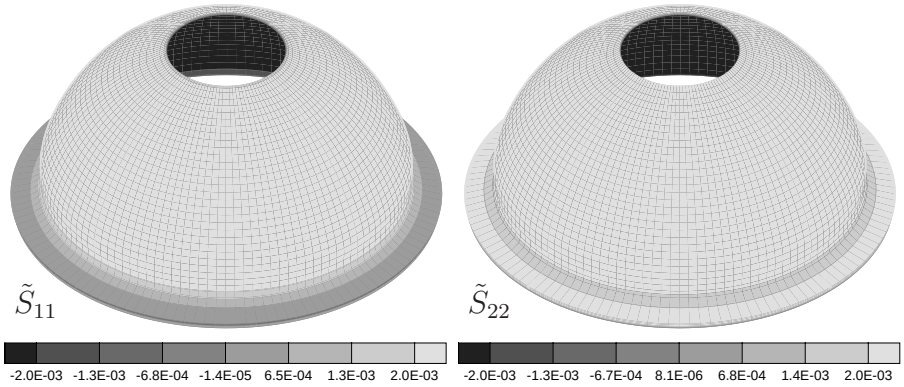

Figure 20: Deformed configuration scaled with an amplification factor 10^3 and plots of the meridian and circumferential stresses $\tilde{S}_{11}$, $\tilde{S}_{22}$ [MN/cm^2] at the surfaces

lows large deformations and includes the analysis of stability problems. The relevant patch tests, which are well known from structural mechanics, are introduced for multi-field problems in particular for piezoelectric shells. Furthermore some numerical examples show the applicability of the proposed element to geometrically nonlinear and to piezoelectric buckling problems.

Appendix
Numerical model of active control

Piezoelectric materials can be used as sensors or actuators. The sensor sense a strain and provides an electric output signal, which may be used as an input signal for the actuator to control the structural behavior. Here, a negative velocity proportional feedback is used in the analysis, see also [19], [17], [15]. The global Eq. (57) is reorganized in such a way that the displacement degrees of freedom $\boldsymbol{u}$ and the electric degrees of freedom of the sensor and actuator, $\boldsymbol{\varphi}^S$ $\boldsymbol{\varphi}^A$ are completely separated. The global vector of the nodal degrees of freedom reads now $\boldsymbol{v}^T = [\boldsymbol{u}^T, \boldsymbol{\varphi}^{S\,T}, \boldsymbol{\varphi}^{A\,T}]$. For the geometrically

linear case Eq. (57) is rewritten as

$$\begin{bmatrix} \boldsymbol{K}_{uu} & \boldsymbol{K}^S_{u\varphi} & \boldsymbol{K}^A_{u\varphi} \\ \boldsymbol{K}^S_{\varphi u} & \boldsymbol{K}^S_{\varphi\varphi} & \boldsymbol{0} \\ \boldsymbol{K}^A_{\varphi u} & \boldsymbol{0} & \boldsymbol{K}^A_{\varphi\varphi} \end{bmatrix} \begin{bmatrix} \boldsymbol{u} \\ \boldsymbol{\varphi}^S \\ \boldsymbol{\varphi}^A \end{bmatrix} + \begin{bmatrix} \boldsymbol{D}_{uu} & \boldsymbol{0} & \boldsymbol{0} \\ \boldsymbol{0} & \boldsymbol{0} & \boldsymbol{0} \\ \boldsymbol{0} & \boldsymbol{0} & \boldsymbol{0} \end{bmatrix} \begin{bmatrix} \dot{\boldsymbol{u}} \\ \dot{\boldsymbol{\varphi}}^S \\ \dot{\boldsymbol{\varphi}}^A \end{bmatrix} + \begin{bmatrix} \boldsymbol{M}_{uu} & \boldsymbol{0} & \boldsymbol{0} \\ \boldsymbol{0} & \boldsymbol{0} & \boldsymbol{0} \\ \boldsymbol{0} & \boldsymbol{0} & \boldsymbol{0} \end{bmatrix} \begin{bmatrix} \ddot{\boldsymbol{u}} \\ \ddot{\boldsymbol{\varphi}}^S \\ \ddot{\boldsymbol{\varphi}}^A \end{bmatrix} = \begin{bmatrix} \boldsymbol{F}^{ext}_u \\ \boldsymbol{0} \\ \boldsymbol{F}^{ext}_\varphi \end{bmatrix} \quad . \tag{60}$$

The sensor is per definition load free, which leads to

$$\boldsymbol{\varphi}^S = -[\boldsymbol{K}^S_{\varphi\varphi}]^{-1}\, \boldsymbol{K}^S_{\varphi u}\, \boldsymbol{u} \quad . \tag{61}$$

For the negative velocity proportional feedback the electric potential of the actuator is defined as

$$\boldsymbol{\varphi}^A := -\boldsymbol{T}_\varphi\, \dot{\boldsymbol{\varphi}}^S \;=\; \boldsymbol{T}_\varphi\, [\boldsymbol{K}^S_{\varphi\varphi}]^{-1}\, \boldsymbol{K}^S_{\varphi u}\, \dot{\boldsymbol{u}} \quad . \tag{62}$$

Here, $\boldsymbol{T}_\varphi$ is a control gain matrix. Substituting Eqs. (61), (62) in (60) yields

$$\underbrace{[\boldsymbol{K}_{uu} - \boldsymbol{K}^S_{u\varphi}[\boldsymbol{K}^S_{\varphi\varphi}]^{-1}\boldsymbol{K}^S_{\varphi u}]}_{\widehat{\boldsymbol{K}}}\, \boldsymbol{u} + \underbrace{[\boldsymbol{D}_{uu} + \boldsymbol{K}^A_{u\varphi}\boldsymbol{T}_\varphi[\boldsymbol{K}^S_{\varphi\varphi}]^{-1}\boldsymbol{K}^S_{\varphi u}]}_{\widehat{\boldsymbol{D}}}\dot{\boldsymbol{u}} + \boldsymbol{M}_{uu}\ddot{\boldsymbol{u}} = \boldsymbol{F}^{ext}_u \quad . \tag{63}$$

It is noted that $\widehat{\boldsymbol{D}}$ is not symmetric.

References

[1] S. Adali. *Smart Materials and Structures with Control and Design Applications*, pages 1–26. CISM Courses and Lectures No. 429. Springer, Wien/New York, 2001.

[2] S.D. Senturia. *Microsystem Design*. Kluwer Academic Publishers, Boston/ Dordrecht/ London, 2001.

[3] H.-M. Si and C. Cho. Finite element modeling of magnetostriction for multilayered mems devices. *Journal of Magnetism and Magnetic Materials*, 270:167–173, 2004.

[4] D.J. Pines and H. Hiraishi. Special issue on smart materials and structures technology: Application to large civil infrastructure. *Smart Materials and Strutures*, 7:581–743, 1998.

[5] H. Allik and T.J.R. Hughes. Finite element method for piezoelectric vibration. *Int. J. Num. Meth. Eng.*, 2:151–157, 1970.

[6] D.A. Saravanos and P.R. Heyliger. Mechanics and computational models for laminated piezoelectric beams, plates, and shells. *Appl. Mech. Rev.*, 52:305–320, 1999.

[7] A. Benjeddou. Advances in piezoelectric finite element modeling of adaptive structural elements: A survey. *Comput. & Struct.*, 76:347–363, 2000.

[8] M. Kögel and M.L. Bucalem. Locking-free piezoelectric MITC shell elements. In K.J. Bathe, editor, *Computational Fluid and Solid Mechanics*, pages 392–395, Oxford, 2003. Elsevier Science.

[9] M. Bernadou and C. Haenel. Modelization and numerical approximation of piezoelectric thin shells. part i: The continuous problems. *Comp. Meth. Appl. Mech. Eng.*, 192:4003–4043, 2003.

[10] M. Bernadou and C. Haenel. Modelization and numerical approximation of piezoelectric thin shells. part ii: Approximation by finite element methods and numerical experiments. *Comp. Meth. Appl. Mech. Eng.*, 192:4045–4073, 2003.

[11] M. Bernadou and C. Haenel. Modelization and numerical approximation of piezoelectric thin shells. part iii: From the patches to the active structures. *Comp. Meth. Appl. Mech. Eng.*, 192:4075–4107, 2003.

[12] X. Wang and Y. Wang. On non-linear behaviour o spherical shallow shells bonded with piezoelectric actuators by the differential quadrature element method (DQEM). *Int. J. Num. Meth. Eng.*, 53:1477–1490, 2002.

[13] R. Lammering and S. Mesecke-Rischmann. Multi-field variational formulations and related finite elements for piezoelectric shells. *Smart Materials and Structures*, 12:904–913, 2003.

[14] R. Lammering. The application of a finite shell element for composites containing piezo-electric polymers in vibration control. *Comput. & Struct.*, 41:1101–1109, 1991.

[15] S. Zheng, X. Wang, and W. Chen. The formulation of a refined hybrid enhanced assumed strain solid shell element and its application to model smart structures containing distributed piezoelectric sensors/actuators. *Smart Materials and Structures*, 13:N43–N50, 2004.

[16] K.Y. Sze and L.Q. Yao. A hybrid stress ANS solid-shell element and its generalization for smart structure modelling. part i – solid-shell element formulation. *Int. J. Num. Meth. Eng.*, 48:545–564, 2000.

[17] K.Y. Sze, L.Q. Yao, and S. Yi. A hybrid stress ANS solid-shell element and its generalization for smart structure modelling. part ii – smart structure modelling. *Int. J. Num. Meth. Eng.*, 48:565–582, 2000.

[18] K.Y. Sze and L.Q. Yao. Modelling smart structures with segmented piezoelectric sensors and actuators. *Journal of Sound and Vibration*, 253:495–520, 2000.

[19] H.S. Tzou and R. Ye. Analysis of piezoelastic structures with laminated piezoelectric triangle shell elements. *AIAA Journal*, 1:110–115, 1996.

[20] H.S. Tzou and R. Ye. Piezothermoelasticity and precision control of piezoelectric systems: Theory and finite element analysis. *Journal of Vibration and Acoustics*, 116:489–495, 1994.

[21] H.S. Tzou and Y. Bao. Nonlinear piezothermoelasticity and multi-field actuations, part 1: Nonlinear anisotropic piezothermoelastic shell elements. *Journal of Vibration and Acoustics*, 119:374–381, 1997.

[22] H.S. Tzou and Y.H. Zhou. Nonlinear piezothermoelasticity and multi-field actuations, part 2: Control of nonlinear deflection, buckling and dynamics. *Journal of Vibration and Acoustics*, 119:382–389, 1997.

[23] P.F. Pai, A.H. Nayfeh, K. Oh, and D.T. Mook. A refined nonlinear model of composite plates with integrated piezoelectric actuators and sensors. *Int. J. of Sol. and Struc.*, 30:1603–1630, 1993.

[24] Y.-H. Zhou and H.S. Tzou. Active control of nonlinear piezoelectric circular shallow spherical shells. *Int. J. of Sol. and Struc.*, 37:1663–1677, 2000.

[25] H.S. Tzou and Y.H. Zhou. Dynamics and control of non-linear circular plates with piezoelectric actuators. *Journal of Sound and Vibration*, 188:189–207, 1995.

[26] D. Varelis and D.A. Saravanos. Nonlinear coupled mechanics and initial buckling of composite plates with piezoelectric actuators and sensors. *Smart Mater. Struct.*, 11:330–336, 2002.

[27] J.S. Yang. Equations for thick elastic plates with partially electroded piezoelectric actuators and higher order electric fields. *Smart Materials and Structures*, 8:73–82, 1999.

[28] S.V. Gopinathan, V.V. Varadan, and V.K. Varadan. A review and critique of theories for piezoelectric laminates. *Smart Materials and Structures*, 9:24–48, 2000.

[29] A. Benjeddou, J.-F. Deü, and S. Letombe. Free vibrations of simply-supported piezoelectric adaptive plates: An exact sandwich formulation. *Thin-Walled Structures*, 40:573–593, 2002.

[30] S. Miranda and F. Ubertini. Consistency analysis of electroelastic finite element models. In *Proc., 2nd European Conference on Computational Mechanics*, pages CD–Version, Cracow, 2001.

[31] K.Y. Sze and Y.S. Pan. Hybrid finite element models for piezoelectric materials. *Journal of Sound and Vibration*, 226:519–547, 1999.

[32] W. Zeng, M.T. Manzari, J.D. Lee, and Y.-L. Shen. Fully coupled non-linear analysis of piezoelectric solids involving domain switching. *Int. J. Num. Meth. Eng.*, 56:13–34, 2003.

[33] E. Dvorkin and K.-J. Bathe. A continuum based four–node shell element for general nonlinear analysis. *Eng. Comp.*, 1:77–88, 1984.

[34] P. Betsch and E. Stein. An assumed strain approach avoiding artificial thickness straining for a nonlinear 4–node shell element. *Commun. Num. Meth. Eng.*, 11:899–909, 1995.

[35] J.C. Simo and M.S. Rifai. A class of mixed assumed strain methods and the method of incompatible modes. *Int. J. Num. Meth. Eng.*, 29:1595–1638, 1990.

[36] G.A. Maugin. Continuum mechanics of electromagnetic solids. In J.D. Achenbach, B. Budiansky, W.T. Koiter, LauwerierH.A., and L. Van Wijngaarden, editors, *Applied Mathematics and Mechanics*, volume 33. North-Holland Series, 1988.

[37] R Simkovics. *Nichtlineares piezoelektrisches Finite-Elemente-Verfahren zur Modellierung piezokeramischer Aktoren*. PhD thesis, Universität Erlangen-Nürnberg, 2002.

[38] S. Klinkel, F. Gruttmann, and W. Wagner. A robust non-linear solid shell element based on a mixed variational formulation. *Comp. Meth. Appl. Mech. Engrg.*, in press, 2005.

[39] M.J. Loikkannen and B.M. Irons. An 8-node brick finite element. *Int. J. Num. Meth. Eng.*, 20:523–528, 1983.

[40] R.L. Taylor. Feap - manual. *http:\\www.ce.berkeley* $\setminus \sim$ *rlt* $\setminus$ *feap* $\setminus$ *manual.pdf*.

[41] R.H. MacNeal and R.L. Harder. A proposed standard set of problems to test finite element accuracy. *Finite Elemets in Analysis and Design*, 1:3–20, 1985.

[42] H.S. Tzou. Development of a light-weight robot end-effector using polymeric piezoelectric bimorph. In *Conference on Robotics and Automation*, IEEE, 1704–1709, 1989.

[43] K.J. Yoon, K.H. Park, S.K. Lee, N.S. Goo, and H.C. Park. Analytical design model for a piezo-composite unimorph actuator and its verification using lightweight piezo-composite curved actuators. *Smart Materials and Structures*, 13:459–467, 2004.

[44] K.J. Yoon, S. Shin, and H.C. Park. Design and manufacturing of lightweight piezo-composite curved actuator. *Smart Materials and Structures*, 11:163–168, 2002.

[45] N.S. Goo, C. Kim, Y.-D. Kwon, and K.J. Yoon. A review and critique of theories for piezoelectric laminates. *Smart Materials and Structures*, 9:24–48, 2000.

[46] H. Hilber, T.J.R. Hughes, and R.L. Taylor. Improved numerical dissipation for the time integration algorithms in structural dynamics. *Earthquake Eng. Struct. Dyn.*, 5:283–292, 1977.

[47] J.M. Whitney. *Structural Analysis of Laminated Anisotrpic Plates*. PhD thesis, Lancaster, PA: Technomic, 1987.